A closer look at potential exoplanet targets from the Nooitgedacht Observatory

H Vorster

orcid.org/0000-0002-9852-5475

Dissertation accepted in partial fulfilment of the requirements for the degree *Master of Science in Astrophysical Sciences* at the North-West University

Supervisor:	Dr B Letarte
Co-supervisor:	Dr RB Kuhn

Graduation May 2023

27239705

Acknowledgements

I would like firstly like to extend my gratitude to the both National Astrophysics and Space Science Program (NASSP), the North-West University's Centre for Space Research (CSR), and the National Research Foundation (NRF), under the grant UID 149978, for financial support throughout my studies.

I also want to thank the personnel at the CSR, Mrs. Elanie van Rooyen, Mrs. Lee-Ann. van Wyk and Mr, Lendl Fransman, who were always there to help with any administrative issues and made sure we were paid on time. I would also like to mention Prof. Christo Venter who helped to secure funding for my third year.

I would especially like to thank my supervisor, Dr. Bruno Letarte, for his continuous support and advice throughout these three years, the endless trips to Nooitgedacht and the long nights spent there to collect data. I would further like to acknowledge my co-supervisor Dr. Rudi Kuhn who was always there to answer my emails and join the zoom meetings to answer my silly questions.

Thank you to all those who accompanied me to Nooitgedacht, Renier Hough, Rigardt Hug, Robin Wessels and Jax Stevens. The time they spent at Nooitgedacht with me was appreciated greatly.

I am eternally grateful to my family who supported me throughout my studies, phoned me just to say they were thinking about me and kept me in their prayers. I would also like to thank my friends for their support and belief, as well as the coffee breaks and the Friday meetings.

Lastly I want to thank my boyfriend Ernst Ellis. He was always there with an endless amount of support and encouragement and always believed in me. He was always there to listen to my rants and stayed awake until I returned from Nooitgedacht in the early morning hours. He is truly a one-of-a-kind person and I owe him so much.

Thank you to my Lord and Saviour who help me through this demanding time even when I was at my lowest point. Without Him this dissertation would not have been possible.

Abstract

Exoplanet surveys like KELT and TESS often require follow-up observations with a traditional, ground based telescope to confirm whether a potential candidate is indeed an exoplanet or not. The optical telescope at the Nooitgedacht Observatory is ideal for these types of observations.

During a transit event, there is a reduction in the brightness of the star, caused by the planet obstructing the light coming from the star. The amount of light blocked by the planet is called the transit depth, and is expressed in parts-per-thousand. The aim of this study was to determine the minimum transit depth observable with the equipment available at the Nooitgedacht Observatory.

Six observations were conducted on known planetary-systems and one for a potential exoplanet target. The images were calibrated, aperture and differential photometry was conducted and the flux of the target was extracted from the images. The flux was normalised and a transit model fit was applied to the data with parameters found in literature, to obtain light curves.

The resulting models and light curves of the transit events are presented. From the models the radius of the exoplanet, the stellar density of the host star and the inclination angle of the planetary-system were determined, which were compared to results found in literature. From the accuracy of the models obtained, it was concluded that the soft limit for the minimum transit depth an exoplanet candidate can have to be detected by the Nooitgedacht telescope, is 10 parts-per-thousand. The hard limit could not be determined due to observational issues. During the course of the project, issues regarding the pointing, tracking and focus of the telescope came to light and recommendations were made on how the issues could be resolved.

Keywords: Nooitgedacht Observatory; exoplanet; transit event; transit depth; light curve

Contents

List of Figures

List of Tables

Table of abbreviations

List of abbreviations used throughout the text.

FOV	Field of view
SNR	Signal-to-noise ratio
ETD	Exoplanet Transit Database
AIJ	AstroImageJ
CCD	Charged Coupled Device

Chapter 1

Exoplanets and the Nooitgedacht Observatory

1.1 Exoplanets

Humans have long been asking whether we are alone in the universe and whether life exists on other planets in other solar systems. We therefore look towards exoplanets for an answer. An extrasolar planet, or exoplanet, is any planet outside of our solar system. Most exoplanets orbit stars, but there are free-floating planets as well that orbit the galactic centre, these are called rogue planets. The first exoplanet orbiting a sun-like star, 51 Pegasi-b, was discovered in 1995 by using the radial velocity method (Mayor and Queloz, 1995). Since this discovery there has been a growing interest in the search for more exoplanets and the possibility that these planets might be inhabited by other life forms.

As of October 2022, 5 171 exoplanets have been confirmed and almost 9 000 candidates have yet to be confirmed. Various methods of detecting and confirming exoplanets have been developed (Akeson et al., 2013); this includes radial velocity, transit techniques, microlensing, direct imaging and astrometry. Figure 1.1 shows the number of planets discovered per year and by which method they were detected. The different methods are best suited for different types of planetary systems. According to Fischer et al. (2015), the transit and radial velocity methods are better with observing larger and heavier planets with a smaller orbit around the host star, whilst the other three methods are better suited to planets in wider orbits. From 2020, as per figure 1.1, it can be seen that the transit method has become the most successful method of detection. This is also the method that will be used in this study.

As seen in figure 1.1 the two most used methods are the transit and radial velocity methods. The radial velocity method relies on the fact that a host star will experience reflex motion due to the gravitational star-planet interaction. Because of this interaction the spectral

lines of the host star will be shifted due to the Doppler Effect. This shift can be detected by using a spectrometer and through the periodic redshift and blueshift the mass of the planet can be estimated.

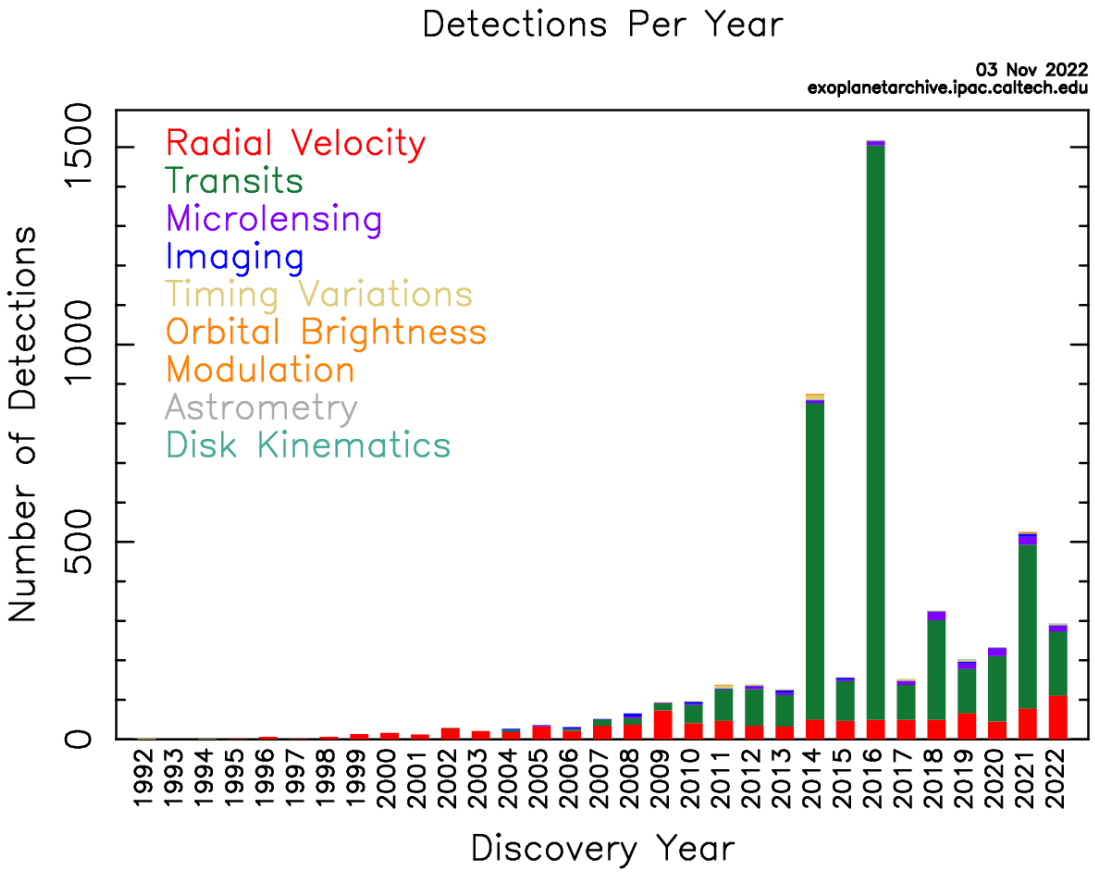

Figure 1.1: Number of exoplanets detected by various methods per annum as per graph extracted from the NASA Exoplanet Archive: `https://exoplanetarchive.ipac.caltech.edu`.

The transit method entails observing a host star for a long period of time as the planet moves across the disk of the star. A decrease in the flux of the star will be observed, as the planet blocks the incoming photons of the star. A light curve is then plotted showing the magnitude of the star over time. This method will be discussed in full detail in section 2.1.

These two methods go hand-in-hand when determining certain parameters of an exoplanet-system. Since both these methods prefer larger planets in smaller orbit, both of them can be used to determine the parameters of one system. By using the transit method, the radius of the exoplanet can be determined, and with the radial velocity method the mass of the planet can be determined. Planetary-systems that have been investigated by using both of these methods are some of the best characterised planets (Charbonneau et al., 2006).

The process of detecting an exoplanet, through the transit method, usually starts with

large surveys that observe large areas of the sky and simultaneously monitor thousands of stars over a long period of time. These can be space-based or ground-based. The Hungarian-made Automated Telescope Network (HATNet) (Bakos et al., 2004), Wide Angle Search for Planets (SuperWASP) (Pollacco et al., 2006) and Kilodegree Extremely Little Telescope (KELT) (Pepper et al., 2007) are ground-based surveys. The Transiting Exoplanet Survey Satellite (TESS) (Ricker et al., 2014) is a space-based survey that was launched in 2018. Light curves are constructed for selected stars to record brightness over time to identity variability and/or periodicity. Analysis of the light curves can reveal the reason of the change in brightness, whether it is a variable star, a binary system or the presence of a planet. Sometimes it is not that clear and follow-up observations are needed from a different type of telescope. This is usually done by smaller, ground-based telescopes which focus on one star (Ricker et al., 2014). These follow-up observations are also performed to determine, with more accuracy, the stellar and planetary parameters, for example the radius, mass, stellar type and effective temperature of the host star and the radius, inclination angle and the orbital period of the planet.

If an exoplanet is detected, the stellar and planetary parameters of the exoplanet system are determined through data reduction and the results are published. New discoveries are added to archives like the NASA Exoplanet Archive (Akeson et al., 2013). This data is used by databases to find observable exoplanets from a given location at a given time. The Exoplanet Transit Database (Poddaný et al., 2010) and the TAPIR: Transit Planning and Reconnaissance (Jensen, 2013) were used in this project to find exoplanets to observe from the Nooitgedacht Observatory.

The nomenclature of exoplanets is very simple; it is usually named after the instrument or project that was used when it was discovered. The first part of the name indicates what star the planet is orbiting, whilst the lower case letter indicates the order in which the planets were discovered in a multi-planetary system. The first planet detected around a star will always be denoted with a lower case b. As an example, WASP-80 b was discovered by the SuperWASP project and it is the first planet that was discovered orbiting the star WASP-80.

1.2 The Nooitgedacht Observatory

The North-West University's Nooitgedacht Observatory is located approximately 35km outside of Potchefstroom, South Africa on the outer edge of the Vredefort Dome. It is situated 1448 metres above sea level and located at 26°54'0.09" S, 27°10'0.05" E. The equipment at the observatory is shown in figure 1.2.

The telescope used is a Meade LX200 16" f/10 ACF Schmidt-Cassegrain telescope, which features a 406 mm mirror with a focal length of 4064 mm and a resolving power of 0.285 arc-seconds. The telescope is mounted on a Paramount ME German equatorial mount, and is controlled by TheSkyX astronomy software from Software Bisque.

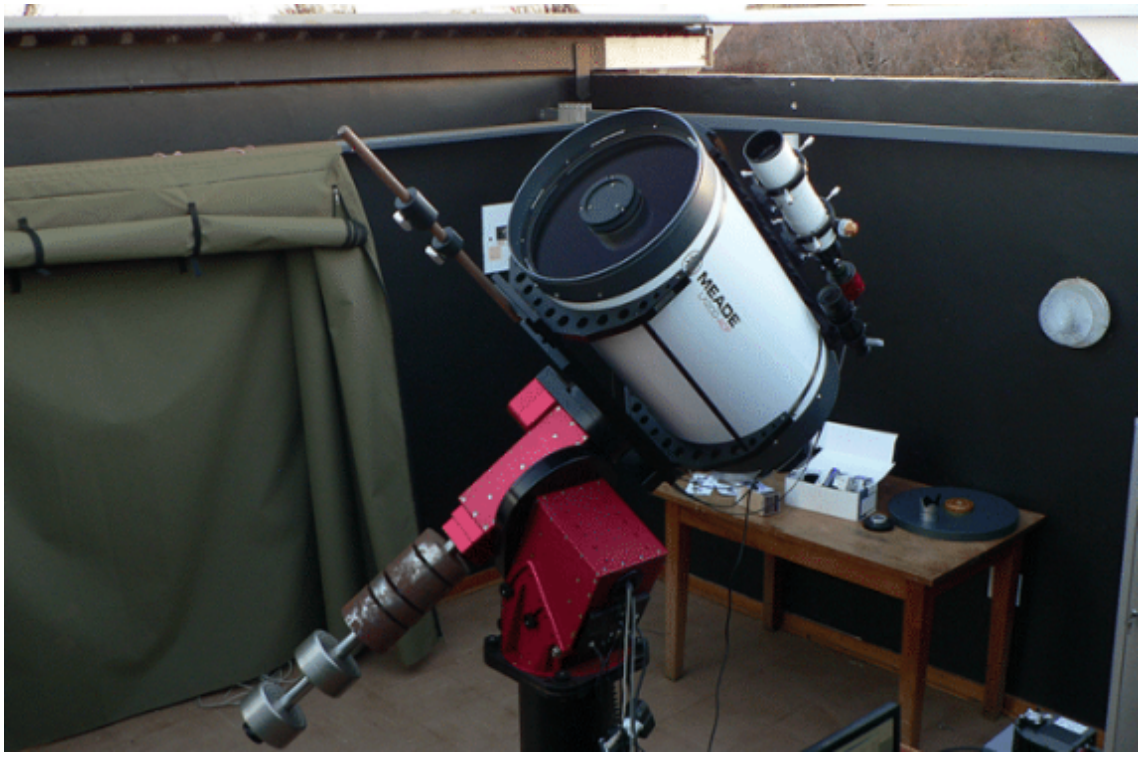

Figure 1.2: Meade LX200 16" f/10 ACF Schmidt-Cassegrain telescope with guide telescope and mount at Nooitgedacht Observatory

The main imaging CCD camera is the Quantum Scientific Imaging (QSI) 540wsi, with a field of view of 15 x 15 arc-minutes . It has internal cooling and can accommodate a filter wheel. Internal cooling is essential in the reduction of thermal noise produced during image capturing. The filter wheel that was used during this study is a Johnson UBVRI Photometric filter wheel; the specifications are shown in table 1.1:

	U	B	V	R	I
Central Wavelength (nm)	365	445	551	658	806
Bandwidth (nm)	66	94	88	138	149

Table 1.1: Johnson UBVRI Photometric Filter specifications

The guiding telescope, a Williams Optics Zenithstar 70 mm Doublet ED APO, is a refracting telescope with a focal length of 420 mm and is attached to the top of the main telescope. The camera connected to the guide telescope is an Atik Titan camera, with a field of view of approximately 30 x 30 arc-minutes. The guide telescope and camera are mainly used for auto-guiding purposes and source finding.

Because of the size and location of the Nooitgedacht telescope, it is well suited to observe exoplanets by using the transit method. As mentioned in Fischer et al. (2015), using the transit method, the exoplanet needs to be in a small orbit, and has to be a Jupiter-sized planet. This means that only certain exoplanets will be suitable for observing. The selection of targets will be discussed in section 3.2.

Chapter 2

Methodology

2.1 Transit Method

The first transiting exoplanet, HD 209458, was found independently by Henry et al. (1999) and Charbonneau et al. (1999). The star was known to have a planetary companion through radial velocity measurements. Henry et al. (1999) and Charbonneau et al. (1999) both did photometric monitoring of the system and observed transit events that coincided with the radial velocity measurements. From this discovery onward there was a rapid increase in the number of discoveries of transiting exoplanets. Some of the discoveries were made by observing exoplanet systems found by the radial velocity method and others by extensive surveys searching for transiting exoplanets orbiting bright stars.

Observing exoplanets with the transit method entails taking a series of images of the host star and the field around it. This happens over the period of time in which the planet passes across the face of the star, including time before and after the start and end of the transit. This method can only be used on the condition that the alignment geometry is suitable for an observer, as shown in figure 2.1. The flux of the host star is extracted from the images and plotted against time. A transit model fit is applied to the data to obtain a light curve, as seen at the bottom of figure 2.1.

To reach the point of obtaining a light curve, the images must first be processed, several external factors influence the flux extracted from the images. The effects of these factors must be rectified before the data is extracted and a model fit is applied. Firstly, the images must be calibrated for any imperfections caused by the CCD camera and the telescope. Secondly the effects of atmospheric extinction, background noise, light pollution etc. must be corrected; this is done by using two techniques: aperture and differential photometry. After the calibration and photometry have been completed, the fluxes of the stars are plotted and a transit model fit is applied.

Transiting exoplanets are of great importance in view of the fact that light curves contain a large amount of information on the planetary system. This includes the square ratio of

the exoplanet radius (R_p) to the host star radius (R_*), the ratio of the semi-major orbital radius (a) to the radius of the host star, stellar density of the host star and the inclination angle (i) (Sing, 2018).

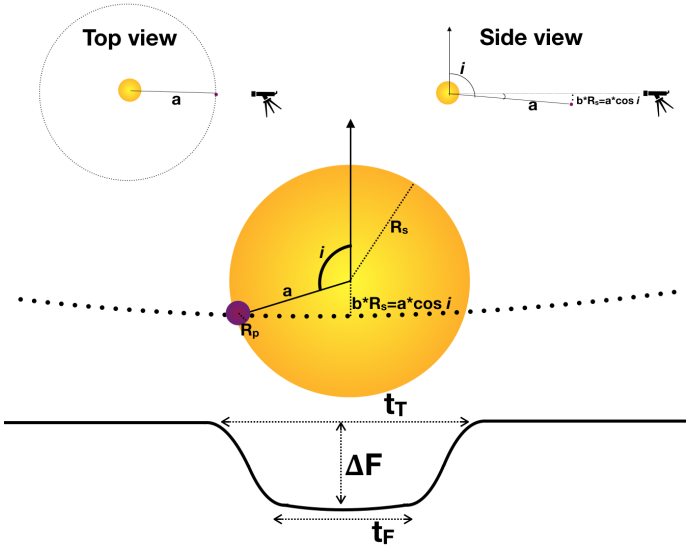

Figure 2.1: Schematic view of observing a transit event courtesy of Deeg and Alonso (2018)

For this research study, known exoplanets will be observed from the Nooitgedacht Observatory. The transit method will be used to obtain a light curve through a transit model fit. The parameters of the planetary system obtained from the model will be compared to the published data on the exoplanet. It will then be established what criteria an exoplanet must fulfil to be observable from Nooitgedacht. Once this has been accomplished the Nooitgedacht telescope can be used in collaboration with large surveys to do follow-up observations as mentioned in section 1.1.

2.2 Data Acquisition

Once a target has been selected, four types of images are taken during the observation. Firstly are the science frames, which are the images taken of the target before, during and after the transit. As mentioned in section 1.1, the raw science images contain noise along with the information of the target field. Unwanted effects, which occur during the observation session and pixel-to-pixel variations due to the CCD camera, contribute to the noise that is captured in the images. The other three images are the calibration images which are used to remove this noise. The three calibration images are flat-fields, dark frames and bias frames (Figure 2.2).

The following sections will explain how these images are captured. The method of choosing exposure times for the science images that will result in the best frames will be discussed, as well as the purpose of each of the calibration images.

2.2.1 Science Images

The first thing to do before starting an observation is choosing the filter/s that is going to be used. In this study the Johnson B- and V- band were mainly used, with occasional uses of the Johnson R- and I-band. These filters were chosen since they are regarded as standard photometric filters. Because the stars in the FOV emit in different wavelengths, the exposure times will be different for each filter. Choosing an exposure time is of utmost importance, if the time of exposure is too long, it may lead to saturated images alternately, a too short exposure time might lead to the image being underexposed. The optimal exposure time maximizes the signal-to-noise ratio (SNR) of the image and the ADU count should be below 75% of the saturation point of the detector.

There are a few other factors that should be considered when choosing an exposure time, other than the filter. Firstly, the seeing conditions on the night of the observation, this will include fog in the atmosphere and atmospheric turbulence. If the moon is very bright and the target is moving away from or towards the moon, the amount of residual light reaching the detector will either increase or decrease and will affect the ADU count throughout the observation. Secondly, whether the star is rising or setting from the local meridian. This means that the light from the star will travel through more or less air. Therefore, if the star is rising, the exposure time has to be reduced to ensure that the image will not saturate later on in the observation. The reverse is true when the star is setting from the meridian.

The process of choosing an exposure time starts with finding the exposure time where the ADU count of the image is at 75% of the maximum ADU count of the detector. The exposure time is then adjusted by taking the above mentioned factors into consideration. The steps are to be repeated for each filter that will be used, and once again, this process should take place directly before the start of the observation.

2.2.2 Calibration Images

Flat fields are taken prior to the observations, after sunset but before it is dark enough for any stars to be visible in the FOV, this technique results in what is called twilight-flats. The flats capture the effect of dust doughnuts and lens vignetting, as seen in figure 2.2a. The doughnuts are caused by any dust that may be present on the lens or mirror of the telescope, or the filters in the CCD camera. These factors reduce the amount of light that reaches the CCD detector. This means certain pixels do not receive the photons that were intended. The flat-fields are taken in every filter that will be used during the observation. The exposure time for this type of image is typically 3 seconds or less, but is also taken when the ADU count is at 75% of the maximum ADU count of the detector.

The next image is the dark frame, this type of image captures the “dark current” that is characteristic of each CCD (Marshall and DePoy, 2013). As seen in figure 2.2b there is

a pattern; this pattern will be present in all of the science images and is caused by the thermal noise from the CCD. The noise is dependent on the temperature of the CCD and the exposure time of the images. These images also capture "hot or cold" pixels. This is why the dark frames should be taken at the same temperature and exposure time as the science images, directly after the observation has concluded. The mirror of the telescope should also be covered so that no photons are able to reach the CCD.

The last image is the bias frame (figure 2.2c). This image contains "read-out" noise that is also characteristic of the CCD (Marshall and DePoy, 2013). The electricity that flows through the sensor of the CCD, when an image is captured, generates this noise. This frame is also taken with the mirror of the telescope covered so that no light can reach the CCD and it should be taken at the lowest exposure time that is possible with the equipment. The CCD camera is capable of capturing zero-second exposures, which is what the bias frames were captured with. These images are also to be taken after the observation has concluded with the CCD at the same temperature.

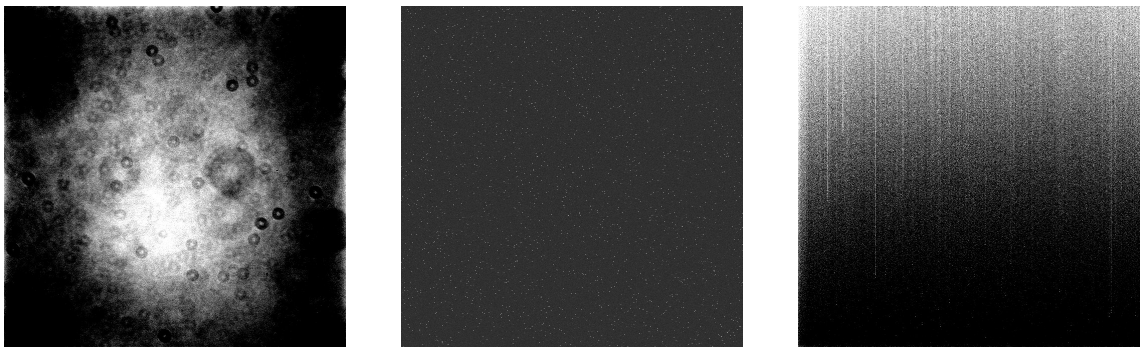

(a) Flat-field (b) Dark frame (c) Bias frame

Figure 2.2: Example of calibration images taken on 27/07/2021 for WASP-80 b

2.3 Data Processing

This section will discuss the three phases of processing the data. To begin with, the data reduction phase, then the photometry phase and lastly the model fitting phase. All three phases were completed by using the application AstroImageJ (AIJ), except for the step where the images were plate solved. AIJ is a public domain, Java-based software package that provides tools for astronomy-specific data processing (Collins et al., 2017). This software was used to conduct the image calibration; and aperture and differential photometry to obtain light curves. AIJ also includes tools for model fitting and light curve detrending. The method described herein was used to process the data of all the observations conducted during this study.

It is important to note that the images are FITS-format files, with a FITS header, containing information on the image/s. This information includes all the details of how and

when the image was captured, the filter that was used, the exposure time; the time at the start of the exposure, the temperature of the CCD, the location of the image, etc. The information stored in the FITS header is used by AIJ to conduct the data processing.

2.3.1 Data reduction

Data reduction includes all the steps taken after the data acquisition and before any photometry is conducted. This involves calibration of the science images and the preparation done on the images for the photometry phase. Before any corrections are made to the images, the stack of images must first be examined to identify whether there are any unusable images. This includes images where there might be cosmic ray hits and satellite or aeroplane trails. If any such images are found they are to be removed from the series, whereafter the image calibration can be conducted.

2.3.1.1 Image calibration

During this phase of the data processing, the signal-to-noise ratios (SNR) of the images are maximized by using the three calibration images discussed in section 2.2, to remove any noise. The first step during this process is combining the bias frames and taking the median of the combined images to create a Master bias. This is then repeated to create a Master dark. Because the bias image captures the ever-present "read-out" noise, this noise will also be present in the dark frames. To remove this noise from the Master dark, the Master dark is corrected with the Master bias. Thus the bias will be removed from the Master dark.

Next a Master flat is created. To create this frame a few steps are required. Firstly, the flat-fields are debiased by subtracting the Master bias. Then a scaling factor is calculated, which is the ratio of the exposure time of the flat fields to the exposure time of the dark frames. The Master dark is then scaled by using this factor and a dark correction is made on the flat-fields. Next the gradient is removed and the calibrated flats are normalised. Lastly the flat images are combined to create the Master flat in the same manner as which the Master dark and bias frames were created. The Master flat is then ready to use.

All science images are calibrated with the Master flat, bias and dark; and the calibrated images are saved. The FITS headers for each of the science images will be updated to include details about the calibration.

2.3.1.2 Plate Solving

Plate solving an image, is the process whereby a relation between the X- and Y-coordinates of the image (pixels from the detector) to positions in the sky (Right Ascension and Declination or RA and DEC), are created. The software will find patterns between the

stars and analyse the distances and angles between sets of four or five stars. It is then compared to information in a database and when a match is found, the World Coordinate System (WCS) information is found for the image. Subsequently, each pixel has a set of X- and Y-values alongside a set of RA and DEC values.

The images need to be plate solved when a meridian flip occurs during the observation session. The German equatorial mount at Nooitgedacht cannot move from East to West over the local meridian. If the target moves through the meridian during an observation, a meridian flip must be executed. The mount is flipped around so that the observation can continue. This results in the telescope with the CCD repositioning and the images will be flipped 180°. The images have to be calibrated by means of plate solving in order to continue with the photometry phase. During the photometry phase, it is crucial that AIJ is always capable of locating the stars by using the WCS information.

The telescope at Nooitgedacht has a problem with tracking stars during long observations. During a long observation, the target star does not remain in the same position on the image, and a drift can be observed in the series of images. Figure 2.3 shows the drift that occurred during a 172 minute long observation. This means that plate solving of all the science images will be required for all observations done throughout the course of this research study.

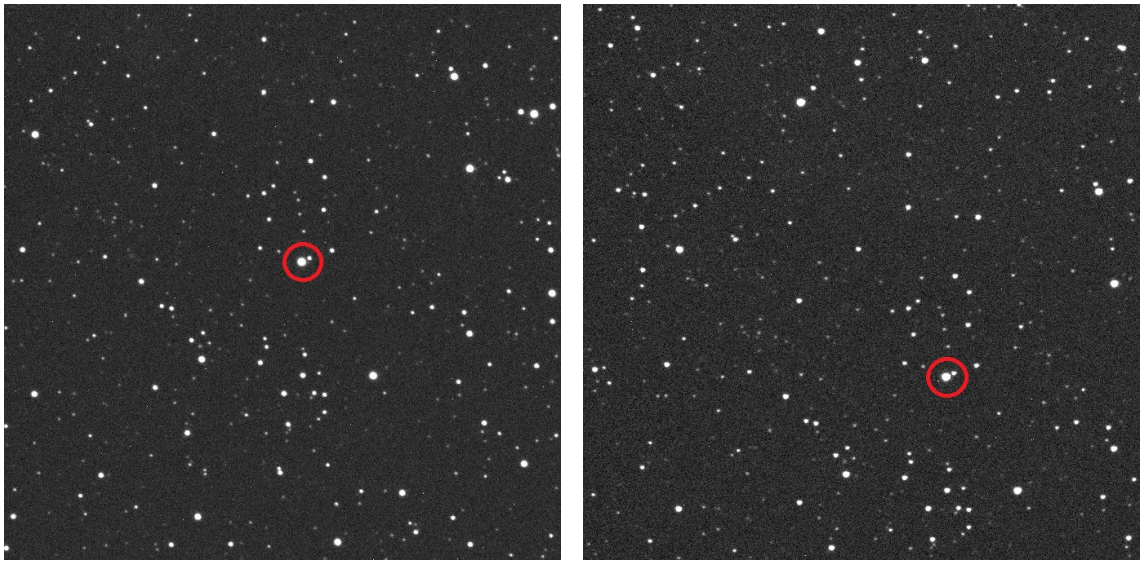

Figure 2.3: These figures show the drift that can occur during an observation. The image on the left was the first image taken of WASP-80 b (shown in the red circle) on the 27th of July 2021 at 21:07:59 SAST and the image on the right was the final image taken at 23:59:57 SAST on the same date.

For this project a local installation of Astrometry.net (Lang et al., 2010) was used. This is a code that performs automatic plate solving on given images. A set of index files were obtained from Astrometry.net, and stored on a local computer. The code extracts sources

(stars) from the images and creates what is called “geometric hash codes” for the sets of stars. The system then searches through the index files to find a “hash code” match. When a match is found the WCS information is added to the FITS header of the image, and each X- and Y-coordinate in the image is assigned a RA and DEC coordinate.

2.3.2 Photometry

Photometry is the measurement of the brightness, also known as the flux, of stars. As has been established in section 2.1, the flux of a host star must be obtained to plot the transit event. To obtain the corrected flux of the host star two photometry techniques are used. The first is aperture photometry, during this step the flux of stars are adjusted to compensate for background sky contribution. The second technique is differential photometry. This technique uses the flux of comparison stars (non-variable stars in the FOV) to correct the flux of the host star which is influenced by common external factors. These factors include moon glow, light pollution and thin cloud coverage. The two photometry techniques are executed simultaneously on the series of images and the results of this phase are added to a measurement table.

2.3.2.1 Aperture photometry

To obtain the flux of a star, an aperture is drawn around the star and the total counts inside the aperture are determined. The sum of the counts is the flux of the star. As can be seen from figure 2.4a the aperture around the star includes some of the background. It would be expected that no counts would be present from the background, but that is not the case. There is background sky contribution that influences the number of counts in the aperture; this background contribution can be due to light pollution or incoming light from the moon. To remove these counts an annulus is also drawn around the star (figure 2.4a), the ADU count per pixel is determined for the area in the annulus. This ratio is used to adjust the ADU counts inside the aperture, and only the counts attributed to the star are left. The amended counts values for the target and comparison stars are saved in a measurement table; and are used during differential photometry.

To determine the radii of the aperture and the annulus, AIJ is used to plot a radial profile for the host star. This is a plot that shows the averaged radial profile of a selected object, and suggests the radius for the aperture and the inner and outer radii for the annulus, in pixels. An example of a radial profile is shown in figure 2.4b. Aperture photometry is also implemented on the comparison stars to determine their flux, but the radii values of the target star are used. This is to ensure the same fraction of background sky contribution is captured in the annulus to correct for the same fraction in the aperture.

The plot also shows the half-width at half-maximum (HWHM) and in the title the full-width at half-maximum (FWHM) can be found, this is used by AIJ to calculate the

suggested radii in pixels. The radius of the aperture is calculated as 1.7 × FWHM. The inner radius of the annulus is calculated as 1.9 × FWHM and the outer radius as 2.55 × FWHM.

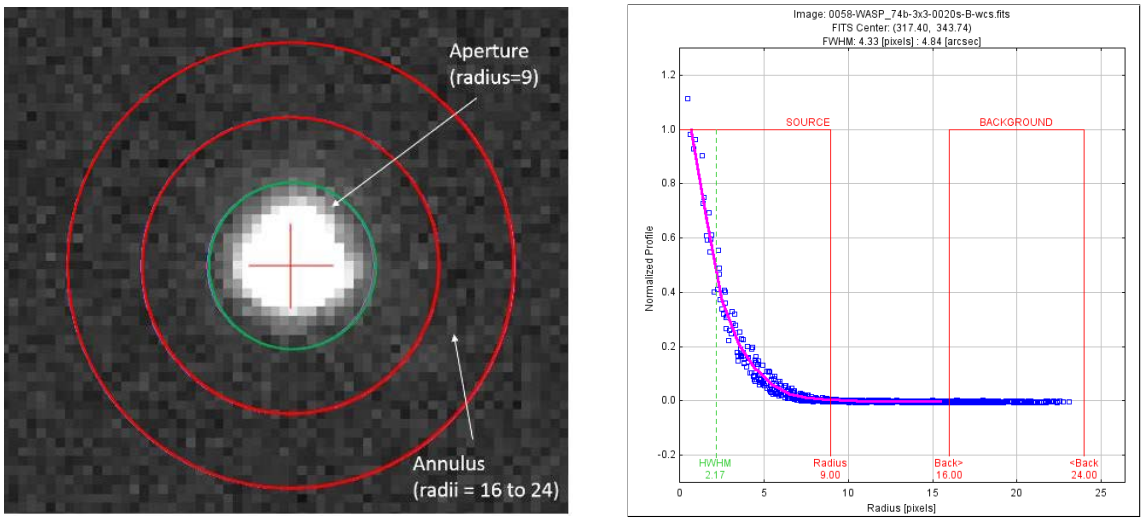

(a) Aperture and Annulus drawn around a star

(b) Radial profile of WASP-74

Figure 2.4

2.3.2.2 Differential photometry

When an extended observation is conducted, with a multitude of images, differential photometry must be used to determine and correct observational variables that have an influence on the ADU counts. This include the effect of atmospheric extinction, as the light from a star travel through the earth's atmosphere the light diminish before reaching the detector. The extinction of the light is correlated with the airmass, the amount of atmosphere that the light has to travel through before reaching the detector. The airmass is measured and added to the FITS header of each image taken throughout an observation. During the observation something like a thin cloud moving over the telescope can also affect the ADU counts captured by the CCD. These and other effects will be captured across the entire FOV.

Differential photometry entails selecting comparison stars that are inherently non-variable and normalising their flux to fit a straight-line model. The relative change made in their flux to fit the model is then used to correct the flux of the target star to negate the variations due to such external factors.

When choosing comparison stars, it is important to select as many comparison stars as possible. The aforementioned increases the accuracy of the factor by which the flux of the target star will be adjusted. It is of equal importance that the comparison stars are inherently non-variable. When a star is selected that is a variable star, it can be removed

later and the calculations will be redone. The comparison stars should also be in the same magnitude range as the magnitude of the target, if this is not possible an ensemble of comparisons stars need to be chosen so that the average ADU counts of all comparison stars are as close as possible to that of the target star.

AIJ has a function that automatically chooses comparison stars based on criteria set by the user. This includes a minimum and maximum peak ADU value and a percentile that the brightness of the comparison star can be above or below the brightness of the target star. After the adjustments are made to the flux, the results are added to the measurement table. This table is used in the next phase to plot the light curve.

2.3.3 Model Fit

2.3.3.1 Understanding the multi-plot

The multi-plot is created with the measurement table from the photometry phase. An example of the plot is shown in figure 2.5. The heading of the plot shows what target the data represents, and the filter and exposure time of the images.

The time axis is given in geocentric Julian date and the dots represent the individual photometric data points. Each point is plotted on the Julian date at the middle of the exposure. The y-axis represents the normalised relative flux of the target (blue dots). Every other data set is shifted from this point.

The relative flux of the target star is plotted twice. The first set is the normalised relative flux (rel_flux_T1), the second set is also the normalised relative flux but it has been adjusted with selected detrend parameters and the data was fitted to a transit model. (rel_flux_T1 Transit Model). The legend shows which detrend parameters were chosen to optimise the model fit; in this case only airmass was selected. A thorough explanation of the selection of the detrend parameters and how they are noted in the legend will be given in the next section.

The next three data sets are the light curves for the comparison stars (rel_flux_CX). These data sets are all normalised and detrended with airmass. The comparison stars data is fit with a constant brightness model, because it is assumed that there would be no relative changes in the flux of these stars. The data points are also binned with a bin size of two for plotting purposes.

The airmass is shown by the brown line, and is arbitrarily scaled and shifted, it is also plotted inversely. The other data set (tot_C_cnts) is the sum of all the ADU counts that were subtracted from the apertures of the comparison stars (refer to section 2.3.2.1). These two data sets should, in ideal conditions, track each other. This is the reason why the

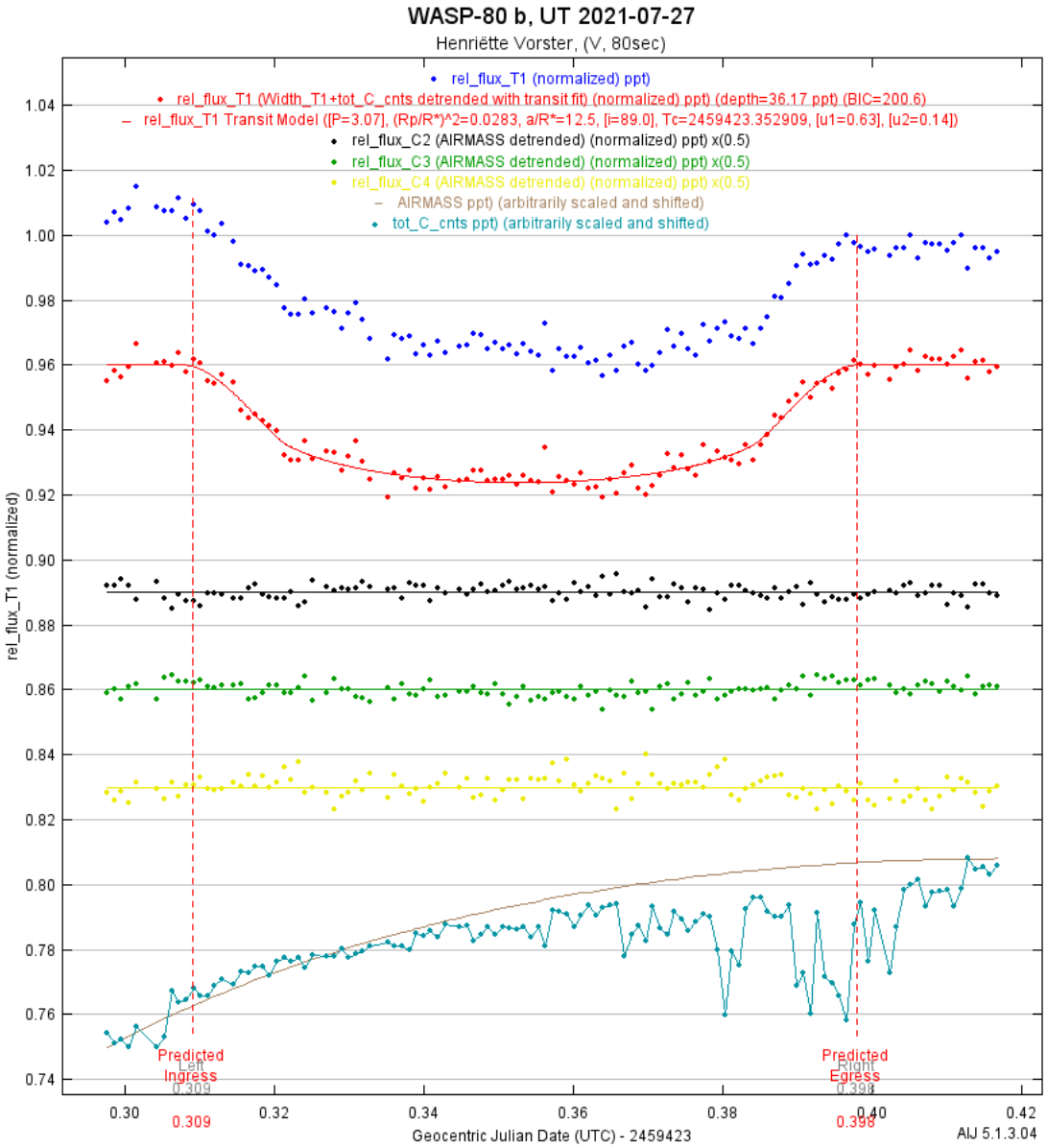

Figure 2.5: Multi-plot for WASP-80 b

airmass is plotted inversely.

The red dashed lines represent the predicted ingress and egress times of the transit. These values are obtained from the Exoplanet Transit Database (Poddanỳ et al., 2010) and TAPIR: Transit Planning and Reconnaissance (Jensen, 2013), where the targets were found. The grey dashed lines represents the ingress and egress points of the transit according to the model. In figure 2.5 the grey dashed lines are not visible since they coincide with exactly with the red dashed lines.

2.3.3.2 Conducting the model fit

The fit that AIJ applies to the data, models the transit as "...an eclipse of a spherical star by an opaque planetary sphere." (Collins et al., 2017). The predicted ingress and egress times are entered and the markers are added to the plot. The markers that represent the ingress and egress points according to the model are also added to the plot, but at the same time as the predicted points. The data outside this region is selected as a normalisation region. A baseline is constructed from this region and it is used to calculate the relative normalised flux for the rest of the data during the model fit. The other parameters used in the creation of the model are: the orbital period, the radius of the host star, the impact parameter and the quadratic limb darkening coefficients.

Limb darkening is an optical effect where the stellar disk of a star appears to be non-uniform in brightness. There appears to be a gradual decrease in brightness from the centre to the edge, the "limb" of the star. This effect occurs because an observer sees the deepest layers of the star at the centre of the star; and only the outer layer of the atmosphere is seen at the limb of the star. The limb darkening coefficients are used to model the effects of limb darkening on the stellar disk to obtain a better model for the transit. This is especially important for the ingress and egress points of the transit model.

The impact parameter (b) is defined as the projected distance between the centre of the host star and the centre of the exoplanet when they are in conjunction. This parameter is used when calculating the orbital inclination (i) of the system. Figure 2.6 shows how the impact parameter is calculated through simple geometry.

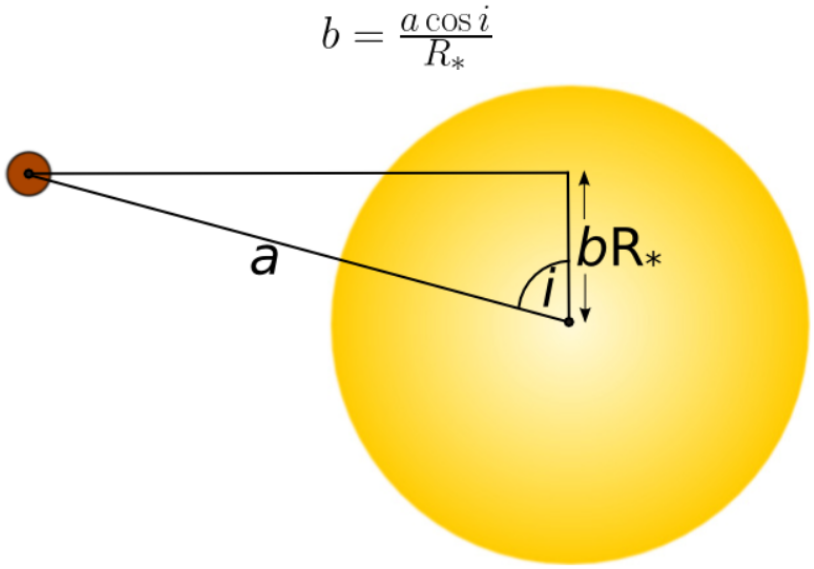

Figure 2.6: Schematic view of how the impact parameter is calculated (Haswell, 2010)

The orbital period, radius and impact parameter are obtained from The Extrasolar Planets Encyclopaedia (Schneider, 2007) and the coefficients are obtained from EXOFAST, a

web-based limb darkening coefficient calculator (Eastman et al., 2013). To calculate the coefficients the calculator needs the filter the images were captured in, the metallicity, effective temperature and the surface gravity ($\log g$) of the host star. These values were found in various papers about the exoplanet system in question. A model fit is then created in accordance with the entered parameters.

The next step is selecting detrend parameters to see if the fit will be improved. Detrend parameters are measurements which may correlate to anomalies in the light curve plot. The values of these parameters are found in the measurement table and are calculated automatically by AIJ. The possible detrend parameters used are:

1. AIRMASS: This value is obtained from the FITS header of each image, and it is the expected airmass at the location of the observation.
2. Width_T1: Due to changes in the seeing conditions during an observation, the point-spread function of the target star can change for each image in the series. This value is a measurement of these changes.
3. Sky/Pixel_T1: This value is the change in the measurement of the background sky contribution, as measured in the annulus of the target star.
4. X(FITS)_T1: This is a measurement of the shift of the target star on the X-axis of the image.
5. Y(FITS)_T1: This is a measurement of the shift of the target star on the Y-axis of the image.
6. tot_C_cnts: This the total background sky contribution counts of all the comparison stars.
7. CCD-TEMP: This is the change of the temperature of the CCD camera during the observation, also found in the FITS header.
8. BJD_TDB: This parameter represents the Barycentric Julian Date in Barycentric Dynamical Time and is used if there is a specific trend in the data specifically due to a long observation.
9. Meridian_Flip: When this parameter is selected AIJ normalises the data taken after the flip occurred in order to take care of any anomalies in the data due to the stars moving to a different part of the CCD.

The best fit is found by minimizing the Bayesian Information Criterion (BIC) and the χ^2 value (Collins et al., 2017). The BIC value is calculated as follows, where k is the number of fitted parameters and N is the number of data points:

$$BIC = \chi^2 + klnN \tag{2.1}$$

Airmass should be selected first as a detrend parameter, and then any number of other detrend parameters can be selected to see if it improves the fit. If a certain detrend parameter is selected, and the BIC value decreases by 2.0 or more, that parameter should be included in the model fit. If the value increases or decreases by less than 2.0, that parameter should not be included. Each detrend parameter is selected, with the airmass; and the effect on the BIC value is checked. After this process the airmass parameter is deselected to see whether the BIC value increases, if it increases by more than 2.0 it should be kept, otherwise it should be omitted. Since the effect of atmospheric extinction is addressed during differential photometry, deselecting the airmass when it does not have a significant effect on the BIC value does not impact the validity of the data.

The detrend parameters that decrease the BIC value the most, will then be selected to include in the model fit. The meridian flip detrend parameter should always be selected if a flip occurred during the observation; and the flip time should be included in the light curve plot.

After the selection of detrend parameters, the position of the markers that represent the ingress and egress points according to the model, should be amended to coincide with the changes to the model due to the selection of detrend parameters. The position of the markers are estimated by eye from the lightcurve. These markers will have an influence on the model fit, since AIJ takes the data outside of these markers to determine the baseline flux. When the markers are moved, the BIC-value will also change.

2.3.3.3 System properties calculated from the fit

When the best model fit is selected, several values are calculated from the fit. Seager and Mallen-Ornelas (2003) derived expressions through basic geometry to relate the quantities obtained from the light curve to the orbital parameters, this includes the radius of the planet (R_p), orbital inclination (i) and the host stars mean density (ρ_*). Figure 2.1 gives a schematic view of a transit event and where some of these values can be found.

Assuming the flux from the planet is negligible, and the host star and planet are spherical in shape, the observed change in flux (ΔF) of the star is proportional to the square of the ratio of the radius of the planet (R_p) to that of the host star (R_*):

$$\Delta F \equiv \frac{F_{\text{no transit}} - F_{\text{transit}}}{F_{\text{no transit}}} = \left(\frac{R_p}{R_*}\right)^2 \tag{2.2}$$

F is defined as the total observed flux. AIJ calculates ΔF automatically from the model, and since the radius of the host star was entered, the radius of the planet is only constricted by the accuracy of the data and the model fit. The orbital inclination, i, is defined as the angle at which the planet orbits the star relative to a reference plane, where this reference plane is perpendicular to the observer's line of sight. This angle is calculated with the

following equation where b is the impact parameter and a is the orbital semi-major axis:

$$i = cos^{-1}\left(b\frac{R_*}{a}\right) \tag{2.3}$$

The dimensionless ratio, a/R_*, can be directly obtained from the photometric data. This ratio is calculated as follows, where t_T is the total duration of the transit and P is the orbital period of the exoplanet:

$$\frac{a}{R_*} = \left[\frac{\left(1+\sqrt{\Delta F}\right)^2 - b^2\left[1-\sin^2(t_T\pi/P)\right]}{\sin^2(t_T\pi/P)}\right]^{1/2} \tag{2.4}$$

This ratio is also calculated by AIJ and used in the calculation for the stellar density, where P is the orbital period and G is the universal gravitational constant:

$$\rho_* = \frac{3\pi}{GP^2}\left(\frac{a}{R_*}\right)^3 \tag{2.5}$$

The values of R_p, i and ρ_* will be compared to the values reported in literature. The value of the ratio a/R_* will also be reported on, since two of the equations are dependent on its value. The radius of the exoplanet is the most important value to be focused on since it is directly related to the transit depth; for this study the minimum depth a transit event can have, in order to be observable from Nooitgedacht, needs to be determined.

Chapter 3

Observations at Nooitgedacht

A total of 9 observations were made at Nooitgedacht for this study. The targets, dates and transit depths are shown in table 3.1. Only one observation was completed in 2020 due to the strict regulations during the COVID-19 pandemic. Most of the observations were completed in 2021. In 2022 multiple reasons stood in the way of collecting data. This included an extensive amount of load-shedding, a disproportionate amount of bad weather and issues regarding transport to Nooitgedacht. Therefore, only one observation was completed in this year.

This chapter will focus on the Nooitgedacht Observatory and the problems encountered throughout the observations, the process of selecting a target to observe, the observational strategy around the problems and each individual chosen target.

3.1 The Nooitgedacht Observatory

The equipment at Nooitgedacht is afflicted with various issues that may have impacted the data obtained, or hindered the process of obtaining data. The major obstacles will be discussed in this section and the less severe obstacles that occurred during specific observations will be discussed in section 3.4.

There are two main problems at the Nooitgedacht telescope, which cause difficulties when observing. The first is the pointing of the telescope. When the telescope is slewed to a target, the target is supposed to be in the centre of the image. In the case of this telescope the target is usually outside the field-of-view (FOV) and the telescope has to be moved around this area to find the target. TheSkyX software has a component that attempts a pointing solution. This works a lot like plate solving, but instead of solving an image it solves the sky as the telescope observes it at that specific point in time. An image taken live with the telescope is compared to a database to solve the exact coordinates the telescope is pointing towards. While multiple pointing solutions were tried, none were successful in improving the pointing accuracy of the telescope. This indicates a larger

problem with no quick solution.

Just before the last observation of HD 189733 b was made on the 7th of September 2022 it was noticed that the computer's system time was set approximately three minutes ahead of the actual time. Since there is no Internet connection at Nooitgedacht, the computer could not automatically update the time. This also meant that TheSkyX software which controls the telescope had presumed the position of a target incorrectly due to the incorrect input of time. When the time was manually adjusted the pointing accuracy of the telescope was improved, but still not working as it should. The time could not be set precisely by doing it manually and it was impossible to ascertain when the inaccuracy of the time had occurred. This meant that the time stamps added to the FITS headers of previous observations would in all probability also have been incorrect. It was deduced that this inaccuracy was presumably caused by load-shedding and was not a gradual change in time.

The second main problem was the tracking of a star during an observation. The main telescope can track stars at a sidereal rate but when a lengthy observation is needed it is recommended to use the guide telescope. The main purpose of using the guide telescope is to make minor adjustments through the mount to keep the FOV exactly the same throughout an imaging session. The system works by selecting a star in the FOV of the guide telescope and placing cross-hairs on a selected guide star. The guide telescope camera captures an image every few seconds and minor movements of the telescope are made to keep the guide star in the cross-hairs. This will ensure that the target star remains in the same position in the FOV of the main telescope. During observations throughout the course of this project, the drift that occurred from one image to the next being too much for the auto-guiding to keep up with. This meant that, during an extended observation, it was necessary to constantly check that the target star was not drifting outside of the FOV and subsequently also to restart the auto-guiding process every 30 minutes.

There can be multiple reasons as to why the drift occurs. One reason might be that the counterweights of the telescope might have shifted a bit and the telescope was not balanced. The most likely reason for this issue is the problem with the pointing that has an influence on the tracking. Since the telescope cannot accurately point to the entered coordinates, the rate of tracking will be incorrect, even if it is just by a minuscule amount. Another possible reason might be because the guide telescope and the main telescope are not centred on the same spot. If an object is in the centre of an image taken with the main CCD it should be in the centre of an image taken with the guide camera. The guide telescope is attached to the main telescope, as seen in figure 1.2, so that the equatorial mount moves both telescopes at the same rate.

During observations it was also noticed that the telescope went out of focus. As seen in figure 3.1, the stars appear much bigger in the image on the left, and the fainter stars appear as doughnuts. This creates irregularities in the data that can be seen on the light curve. The case shown in figure 3.1 is the most extreme case that occurred during this study, it is probable that the mirror of the telescope was not locked in place

before starting the observation and the mirror gradually started to shift as the telescope moved whilst tracking the star. As for the other observations where the focus only shifted slightly, it is further suspected that it might also have been the temperature drop during the night that caused the metallic gears to shrink, resulting in the shifting of the mirror. The Nooitgedacht Observatory is located very close to the Vaal River and significant temperature drops often occur in the area.

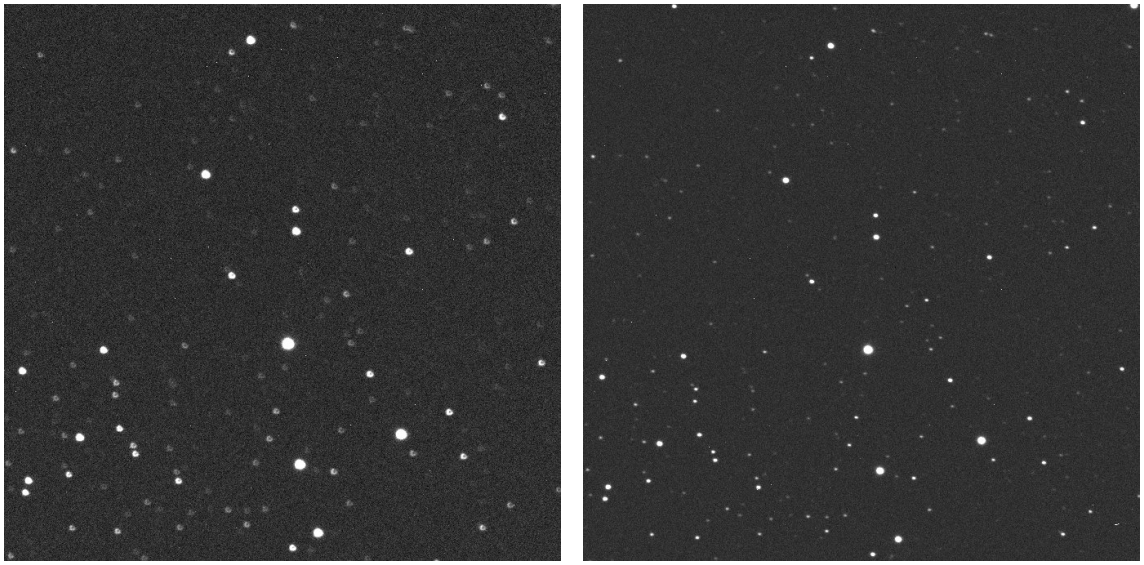

Figure 3.1: Two images taken during the observation of WASP-74 b on the 20th of July 2021. The image on the left shows that the telescope was out-of-focus and the image on the right was taken immediately after the telescope was refocused.

3.2 Selection of Targets

As mentioned in chapter 1.2, only a certain fraction of the known exoplanets can be observed with the transit method. The Exoplanet Transit Database (Poddanỳ et al., 2010) and TAPIR: Transit Planning and Reconnaissance (Jensen, 2013) databases only present information regarding transiting exoplanets; these were the two databases that were used to find the targets to be observed. When the location of an observatory is entered into these databases, it outputs a list of what exoplanets can be observed from that location on a specific date. This list includes information on each of the transit events: the start and end times of the transit, the elevation of the star at the start and end of the transit, the apparent magnitude of the star and the depth of the magnitude change during the transit. These variables are investigated to determine which targets would be the best to observe.

The apparent magnitude is a measure of the brightness of a celestial object as seen by an observer from earth. The magnitude scale works inversely to what would be expected; brighter objects are denoted with a lower and sometimes even a negative value. The Sun

has an apparent magnitude of -26.74 while Uranus has an apparent magnitude of 5.68. The depth of a transit is how much the apparent magnitude of a star changes when a planet is passing in front of the disk of the star. The depth can be given in magnitude, but for this research study, the depth will be denoted by parts-per-thousand (ppt).

Due to the limitations at the observatory, there are a few criteria that a target must meet to be observable from Nooitgedacht. The first criterion is the magnitude of the host star. With the set-up of the telescope and the CCD camera it is possible to observe stars with a magnitude as faint as 15. Due to the lengthy observations needed, a few factors change the minimum magnitude of stars that can be observed, and also imposes a maximum limit. To obtain good quality images for processing, the exposure times will have to be longer for fainter stars. This poses a problem at Nooitgedacht because of the issues with the tracking of the telescope. This means longer exposure times may lead to trailing stars which will render the images unusable. For brighter stars the exposure times will have to be very short to prevent overexposure. This may lead to images with not enough or no comparison stars for sufficient data processing, and therefore start with a magnitude range of 7 to 12.

The second criterion is the depth of the transit, in other words how much the flux of the star diminishes when the planet is in transit. If the change in flux is too small, the light curve does not show the dip; thus the results cannot be interpreted. This is the criterion for which a limit needs to be found for the Nooitgedacht telescope.

In order to obtain a sufficient amount of data for processing, the observation has to start at least 30 minutes prior to the predicted start of the transit (pre-ingress) and end at least 30 minutes after the predicted end of the transit (post-egress). Factoring in the time to set-up the telescope, finding and positioning the star in the field of view (FOV) and choosing exposure times, the start time of the transit has to be no less than 90 minutes after sunset. For transits that occur in the early morning hours, the end of the transit has to be at least an hour before sunrise. This is the third criteria to look at when choosing a target.

Lastly is the elevation of the star at the beginning and the end of the transit. As seen in figure 1.2, the telescope is located inside a building where the roof opens to reveal the night sky. The walls of the building obstruct about 20 degrees of sky from the horizon upwards. The chosen target's start or end elevation, therefore, needs to be at least 30 degrees. This is to allow for the extra observation time before and after the transit ends.

3.3 Observational Strategy

Observations were only made during the optimal observation season. This season is during the winter months, mid-June to late-September. The lower temperature in the winter season ensures that the equipment also maintains a lower temperature, thus ensuring that

the images capture less noise due to less thermal energy being present in the CCD. Colder air also has less moisture which means that the atmosphere is more transparent. The nights are also longer in the winter, there is therefore a larger window of time in which observation can be completed.

A target was identified for each day during the winter season, in accordance with the criteria discussed in section 3.2. From this list, the best targets were identified in accordance with the main aim of this study. After a target was selected, external factors were taken into account, including the weather conditions of that day, the load-shedding schedule and the availability of personnel and transport to the observatory.

On a night when an observation was to be made, the aim was to arrive at the observatory an hour before sunset, thus leaving enough time to unlock and set-up the instrumentation before the twilight flat-fields needed to be captured. The flat-fields would be captured right after sunset, as described in section 2.2.2.

After the flat-fields had been captured, it was necessary to wait until the sky had darkened enough to find the target. The coordinates of the target were entered and the telescope allowed to automatically turn to the required position. As discussed in section 3.1 there is a problem with the pointing of the telescope. Charts that were obtained from TAPIR (Jensen, 2013) were thus found and printed to aid in finding the target. Images were taken with the guide telescope camera and the main CCD. The guide camera was used in place of the main CCD as it has a larger FOV and more stars would thus be present. The aforementioned helps with finding patterns among the stars that can be compared to the finding charts to identify the position of the target star. When the target is found the telescope is adjusted, either by using the joystick or TheSkyX software, to place the target in the centre of the image.

The exposure times are determined as described in section 2.2.1 and the software is programmed to take a series of images throughout the length of the observation. When a target is selected, it is determined beforehand whether a meridian flip would occur during the observation. After a flip occurs, the target might not be in the FOV and the finding charts would need to be used to locate the target again. The telescope is repositioned and the observation can proceed. It is possible for this process to take up to half an hour, which can impact the model fitting, depending on during which stage of the transit event the meridian flip occurred.

After the main observation is complete, the roof of the observatory is closed and the lens cover of the telescope put in place to capture the dark and bias frames. The last images are captured, as described in section 2.2.2 and the data is then transferred to a removable storage device for data processing.

3.4 Observations

This section will discuss the targets that were chosen to observe, table 3.1 shows what targets were observed. It also shows the predictions of the transit: the start, middle and end times, as well as the magnitude of the host star and the depth during the transit. The problems encountered during each observation, that may affect the data, will also be discussed.

Date	Object	Begin (SAST)	Middle (SAST)	End (SAST)	V (mag)	Depth (ppt)	Sunset (SAST)
16/09/2020	HD 189733 b	19:37, 37°	20:31, 38°	21:25, 36°	7.67	24.0	18:02
09/07/2021	WASP-7 b	22:07, 38°	23:54, 61°	01:41, 79°	9.5	6.7	17:33
20/07/2021	WASP-74 b	21:39, 40°	22:48, 52°	23:57, 61°	9.7	9.8	17:38
24/07/2021	HAT-P-57 b	20:41, 43°	22:26, 50°	00:11, 43°	10.4	9.4	17:40
27/07/2021	WASP-80 b	21:25, 44°	22:29, 55°	23:33, 62°	11.881	29.4	17:42
08/08/2021	HD 189733 b	22:43, 38°	23:37, 38°	00:31, 34°	7.67	24.0	17:48
09/08/2021	TOI 392.01 b	03:10, 41°	03:51, 49°	04:31, 56°	8.3	2.85	17:48
10/08/2021	KELT-10 b	20:14, 61°	22:12, 72°	23:58, 62°	10.6	14.2	17:49
07/09/2022	HD 189733 b	20:29, 37°	21:23, 38°	22:17, 35°	7.67	24.0	18:11

Table 3.1: The exoplanet targets that were observed from the Nooitgedacht Observatory.

HD 189733 b

This target has an apparent magnitude of 7.67 and a depth of 24.0*ppt*. This is a fairly bright star with a large transit depth, which made it a very good target to start with. The target was observed on three separate occasions, on the 16th of September 2020, the 8th of August 2021 and the 7th of September 2022.

During the observation in 2020 no problems occurred. The filters that were chosen for this observation were the Johnson B- and V-band. The telescope went a bit out of focus after

the meridian flip, but not severely enough to need refocusing. This meant that the sizes of the aperture and annulus radii were set to larger values so that in the images after the flip, the star was encompassed by the aperture. This would lead to a minor error in the light curve plot.

Since this target had already been observed, with the observation in 2021 it was decided to capture it in the Johnson R-band. The humidity was at approximately 30% and the atmosphere appeared hazy. When attempting to start the observation TheSkyX software was not responding and the program had to be restarted twice before the problem became apparent. When taking a series of images, the software requires an input of how many images should be captured. Since the exposure time was set to 5 seconds, 99999 was input as the amount of images to be captured. This was way too much for the software to handle and the program stopped responding. After this the number was decreased to 1000 and the observation commenced. Due to the delay the observation started at 21:00 and the predicted ingress of the target was at 22:43. The observation was continued despite the delay.

The observation in 2022 proceeded with no complications. It was decided to observe with the Johnson B-band for a comparison with the observation made in 2020. This target was observed utilising the main telescope's sidereal tracking; without the use of auto-guiding. Figure 3.2 shows the drift that occurred from the start of the observation until the last image captured before the meridian flip occurred. The drift throughout the observation is the same as the drift experienced while using the auto-guiding. This meant auto-guiding served no significant purpose.

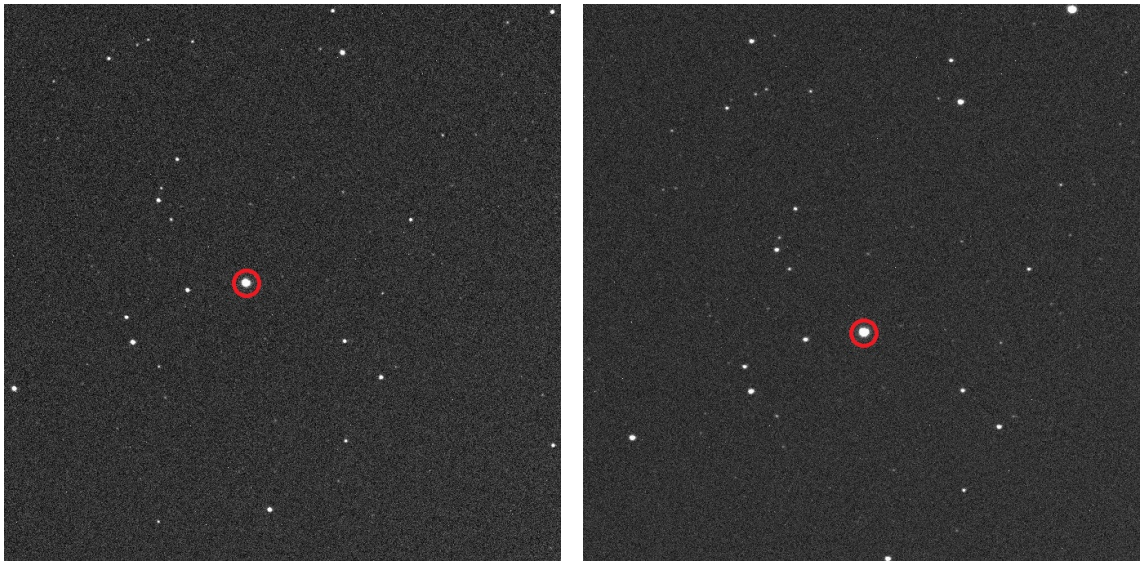

Figure 3.2: The image on the left was taken of HD 189733 b at 19:59 SAST and the image on the right was taken 79 minutes later at 21:18 SAST.

WASP-7 b

This target was selected as the first with a small depth of 6.7*ppt*. The magnitude of the target, 9.5, is also still in the range of the optical capabilities of the telescope. At about 22:30 SAST, just before halfway through the observation, the camera disconnected from the telescope. This happened because the wire that connects the camera to the computer got stuck and it was dislodged. When the camera was reconnected, the telescope was also adjusted because the target was slowly drifting out of the FOV. This caused a small gap in the data. This target was captured in all four filters, the Johnson B-, V-, R- and I-band.

WASP-74 b

This star was chosen because its magnitude is very close to that of WASP-7 b, 9.7 versus 9.5. It also has depth that is a bit larger than that of WASP-7 b, so it would make a good comparison. During the observation at 21:00 SAST it was noticed that the focus of the images were getting worse. The observation was paused and the telescope was refocused. The process of getting the telescope focused only took a few minutes, so not a lot of observation time was missed. In figure 3.1 the difference in the out-of-focus and in-focus images can be seen. The figure shows images taken in the Johnson R-band, this meant that a larger aperture and annulus radii would have to be used and an error in the data was expected. This target was also captured in all four filters.

HAT-P-57 b

The transit depth of this target is very close to that of WASP-74 b, though the magnitude of the host star for this target is fainter. This target was chosen to see how the magnitude of the host star would influence the results for two transits with similar depths. At the start of the observation it was difficult to find the target. Figure 3.3 shows a finding chart that was used to find the target; from this it can be seen that the field around the target is extremely busy. Problems were also encountered with the joystick whilst trying to find and move the target into place. This delayed the start of the imaging session and the first image was only captured at 20:38 SAST, three minutes before the predicted ingress point. During this observation, the Johnson B- and V-band were used.

WASP-80 b

WASP-80 is a very faint star, almost at the imposed limit, but it has a very large transit depth. This target was chosen to support the notion that planetary systems with faint host stars and large transit depths can easily be observed from Nooitgedacht. During observations prior to this one, two or more filters were used. This led to the conclusion that there might not be enough data points to obtain a good model fit if a lot of filters

are used. Therefore, from this point onwards, only one filter was used in the observations. For this observation the Johnson V-band was used and no complications occurred during the imaging session.

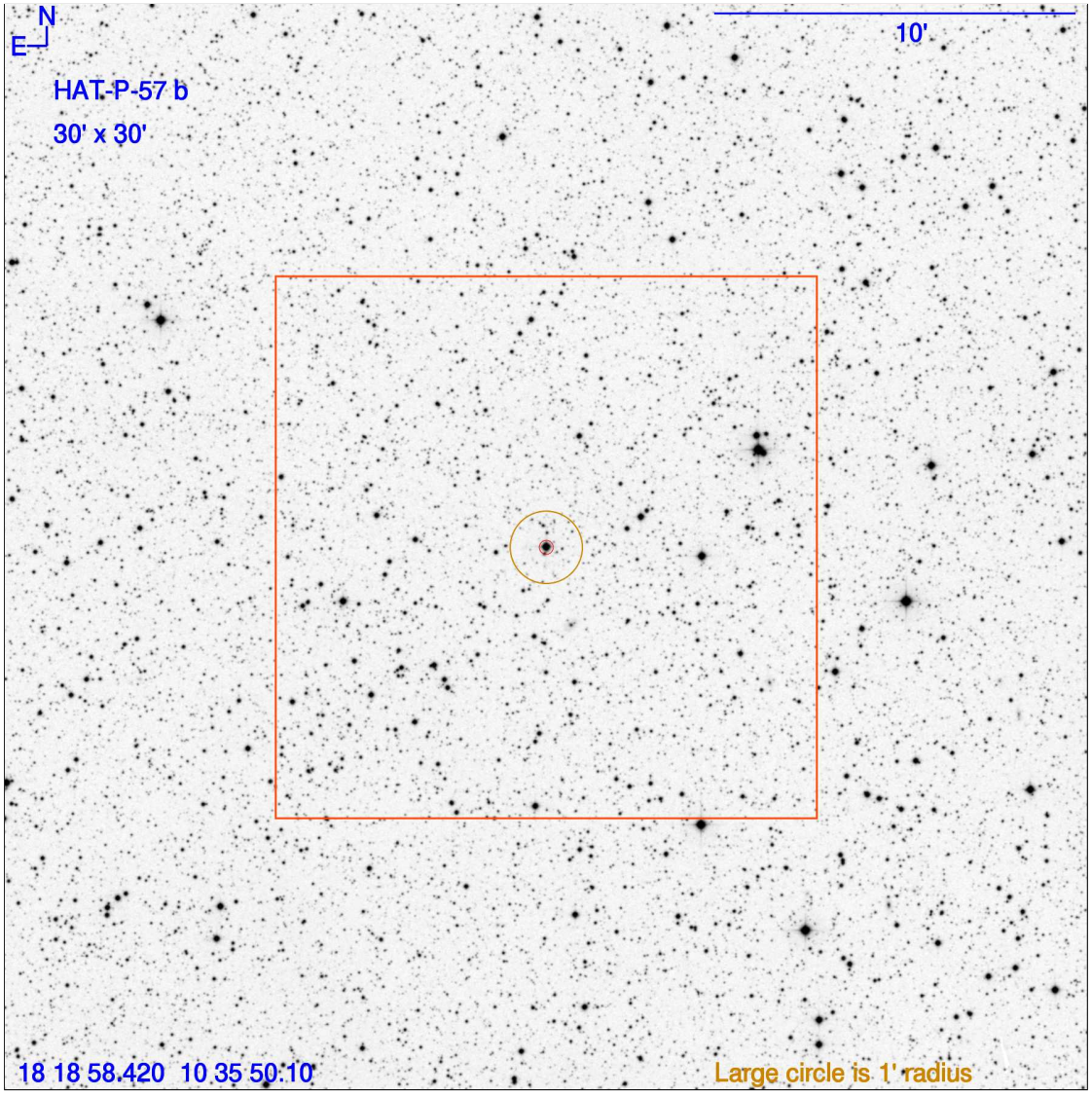

Figure 3.3: This figure is the finding chart for HAT-P-57 b; it shows the field around the target in a 30×30 arc-minute field-of-view (FOV). The red box shows a 15×15 arc-minute FOV, which is the FOV of the main CCD detector.

TOI 392.01 b

This target was chosen because it is a more recent TESS object of interest (TOI); it has not been confirmed as an exoplanet. The magnitude of the host star is in the range of observable magnitudes but the depth of the transit is very small. This target was chosen to determine whether exoplanets with small transit depths could be observed and the data points then binned together to obtain a reliable light curve. It was concluded that it would probably not be possible since the transit depth is extremely small and a reliable light curve would also probably not be obtained. This target was captured on the same

night as HD 189733 b and due to the high humidity that night the atmosphere was foggy. During this observation the Johnson R-band was used.

KELT-10 b

This target was selected because it is a good intermediate target. The host star's magnitude is comfortably in the range of the capabilities of the equipment at Nooitgedacht and the transit depth is small but still observable. This is also a good target to compare with HAT-P-57 b, since the magnitude for both are almost the same, but the transit depths differ by 3.8*ppt*. This observation started 13 minutes before the predicted ingress time and the images were captured using the Johnson B-band.

Chapter 4

Light Curve Analysis

In this chapter the light curves for all the targets that were observed are presented. Table 4.1 gives a summary of the filters and exposure times that were used in each observation, as well as the radii of the aperture and annulus used during the photometry phase. The radial profiles for each data set are given in figure A.1 in Appendix A.

Date	Target	Filter	Exposure Time(s)	Aperture (pixels)	Inner Annulus (pixels)	Outer Annulus (pixels)
16/09/2020	HD 189733 b	B	15	8	14	21
		V	3	8	14	21
09/07/2021	WASP-7 b	B	20	8	14	21
		V	20	7	13	20
		R	20	7	13	20
		I	20	7	13	20
20/07/2021	WASP-74 b	B	20	9	16	24
		V	20	8	14	21
		R	20	8	14	21
		I	20	9	16	24
24/07/2021	HAT-P-57 b	B	25	6	11	17
		V	25	6	11	17
27/07/2021	WASP-80 b	V	80	6	11	17
08/08/2021	HD 189733 b	R	5	9	16	24
09/08/2021	TOI 392.01 b	R	15	9	16	24
10/08/2021	KELT-10 b	B	40	8	14	21
07/09/2022	HD 189733 b	B	9	6	11	17

Table 4.1: Exposure times and radii values for apertures and annuli for each data set.

Each light curve will be accompanied by a table listing the values of the parameters used in the model: orbital period P, radius of the host star R_* and the impact parameter b. The table also shows the following values according to solutions from literature: the radius of the planet, R_p, the inclination angle, i, the stellar density, ρ_* and the ratio a/R_*. It is important to note that the values obtained from literature are also obtained from models. Discrepancies might exist between the different models from different observers. For the sake of consistency, the parameters used in the creation of the model were derived from and will be compared to the same paper as that from which the system-property values were obtained.

For this study it was decided to only calculate the error of the radius of the exoplanet since it is the most important value. The stellar density can be determined with much more accuracy by use of spectroscopic observations. The errors of this value were therefore not calculated since it does not directly assist the main aim of this study.

4.1 HD 189733 b

Since this target was observed on three separate occasions, the results are presented together. The parameters that were used during the model fit for all the data sets, and the system-properties for this target are listed in table 4.2. Three comparison stars were used during photometry and were binned with a factor of two for visual purposes, unless stated otherwise.

Parameter	Units	Value	Reference
P	Period (days)	$2.218577^{+0.000009}_{-0.000010}$	Addison et al. (2019)
R_*	Radius ($R_\odot$)	$0.765^{+0.019}_{-0.018}$	Addison et al. (2019)
b		$0.656^{+0.014}_{-0.015}$	Addison et al. (2019)
System properties			
R_p	Radius (R_{Jup})	1.119 ± 0.038	Addison et al. (2019)
i	Inclination (deg)	$85.69^{+0.095}_{-0.097}$	Addison et al. (2019)
ρ_*	Density (cgs)	2.56 ± 0.13	Addison et al. (2019)
a/R_*		8.73 ± 0.15	Addison et al. (2019)

Table 4.2: Values for HD 189733 parameters and system properties

B-band Light Curve (16/09/2020)

In the light curve for the B-band, figure 4.1, it can be seen that the ingress- and egress-points according to the model have shifted to the right side of the predicted points, and the total time of the transit is also a bit shorter than what was predicted. This could be

due to the fact that this target was observed in 2020 and the original predicted ingress- and egress-points were wrong to begin with, or there was a too large error in the data for the model to be completely accurate. This only had an effect on the inclination angle and stellar density obtained from the model, which will be explained later in this section.

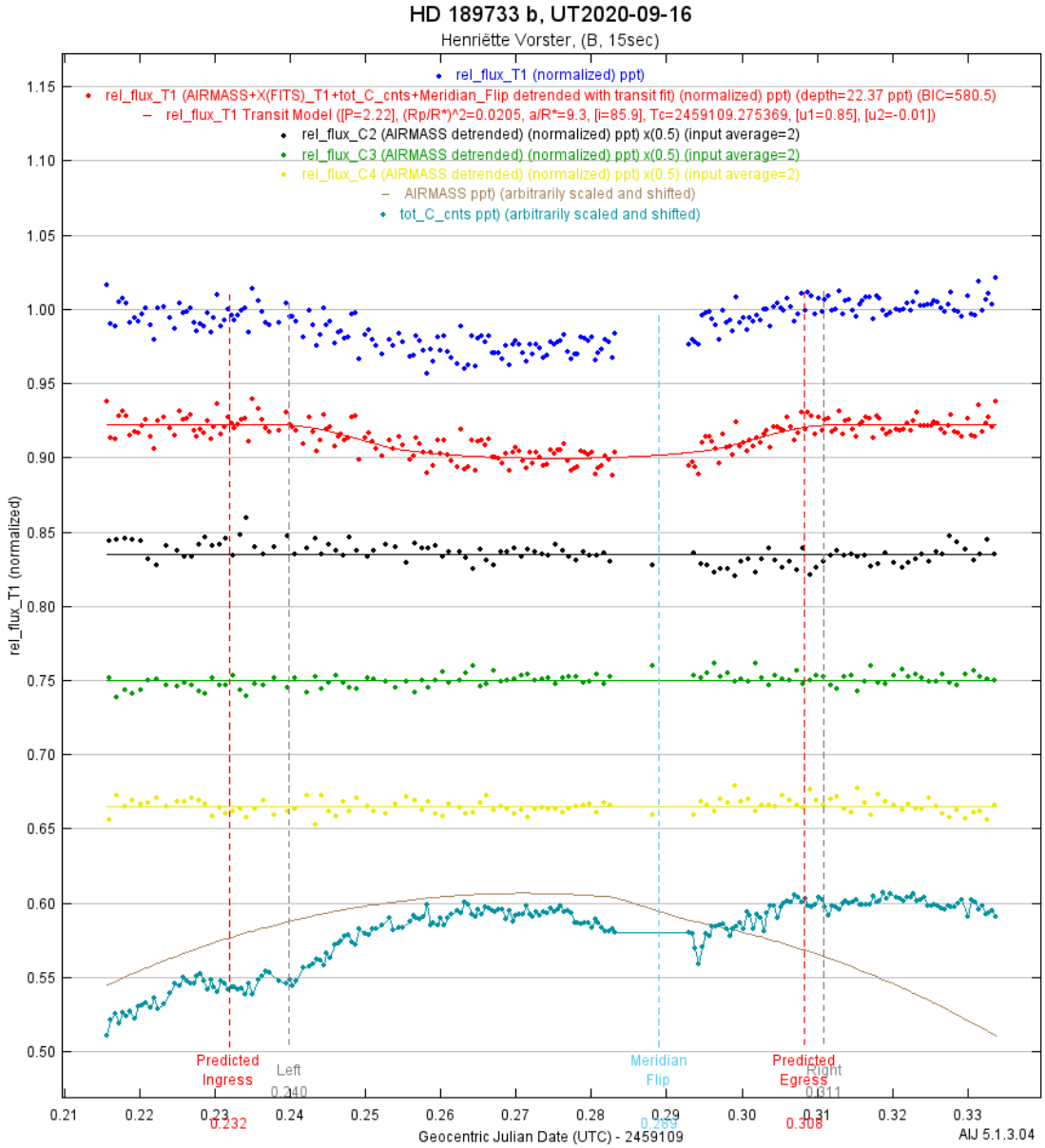

Figure 4.1: HD 189733 b light curve, B-band.

Towards the end of the observation, just before the meridian flip, the telescope gradually went out of focus; as a result the total background sky counts (teal data points) stopped following the trend of the airmass (brown line). The reason for this trend was because when images are out of focus, the stars appear larger in the images; due to this the aperture sizes used during photometry had to be increased. This meant more of the background sky was encompassed within the aperture and the differential photometry process was negatively affected.

Since the targets drift during the imaging session, there are two detrend parameters that will be used frequently: X(FITS) and Y(FITS). These values are measurements of the shift of the target on the axes of the images. For this fit, the X(FITS) detrend parameter was used. The other detrend parameters that were used are: the airmass, the background sky contribution counts and the meridian flip parameter. This combination of detrend parameters gave the lowest BIC-value and thus the preferred model fit (see section2.3.3.2).

The values calculated from the model are given in table 4.3. The radius of the exoplanet, calculated from the model is $R_p = 1.1210^{+0.0265}_{-0.0251}\ R_{\rm Jup}$, while the value found in Addison et al. (2019) is $R_p = 1.119 \pm 0.038\ R_{\rm Jup}$. The value retrieved from the model closely correlates with the value found in literature.

The value for the inclination angle, however does not coincide with the value obtained from literature, as $i = 85.94$ degrees was extracted from the model and the range found in the literature is $i = 85.69^{+0.095}_{-0.097}$ degrees. The calculated value is still close to the range given in literature; this difference is due to ratio a/R_* found in equation 2.3. From the model $a/R_* = 9.2741$, while the value reported in Addison et al. (2019) is $a/R_* = 8.73 \pm 0.15$. In equation 2.4, the ratio a/R_* is dependent on the duration of the transit. Since the duration from the model does not coincide with the predicted duration, the difference in the value for the inclination is thus explained.

The same is true for the calculated value of the stellar density. From the model, $\rho_* = 3.0617$ g/cm^3, but the range given in literature is 2.56 ± 0.13 g/cm^3. This value differs significantly from the range, since the ratio a/R_* is cubed in equation 2.5 and thus led to a large deviation from the value found in Addison et al. (2019).

Properties	Units	Calculated Value	Literature Value
R_p	Radius ($R_{\rm Jup}$)	$1.1210^{+0.0265}_{-0.0251}$	$0.765^{+0.019}_{-0.018}$
i	Inclination (deg)	85.94	$85.69^{+0.095}_{-0.097}$
ρ_*	Density (cgs)	3.0617	2.56 ± 0.13
a/R_*		9.2741	8.73 ± 0.15

Table 4.3: Fit results for HD 189733, B-band (16/09/2020).

V-band Light Curve (16/09/2020)

The transit fit for the data captured in the V-band is given in figure 4.2. The detrend parameters used in the model fit process are: the change in the point-spread function of the target, the background sky counts of the target, the CCD temperature change and the meridian flip.

The duration of the transit was modelled longer than what was predicted, as the egress time had shifted on with approximately 27 minutes. The reason for the inconsistency in

duration of the transit is due to the total background sky counts being more sporadic with the V-band in comparison to the B-band (figure 4.1). The fact that the telescope went out of focus towards the end of the observation is also a factor that influenced the predicted egress-point. The difference between the models for the B- and V-band is explained by the fact that stars emit a different amount of light in different wavelengths. Since the stars in the FOV emitted more light in the V-band range; the exposure time for the V-band was shorter (3 seconds), whilst the exposure time for the B-band was longer (15 seconds). It is not necessarily the target that emitted more in the V-band range, it could also be the comparison stars. This explains the sporadic trend of the total background sky counts in the plot for the V-band data (figure 4.2), which was not seen in the plot for the B-band data (figure 4.1).

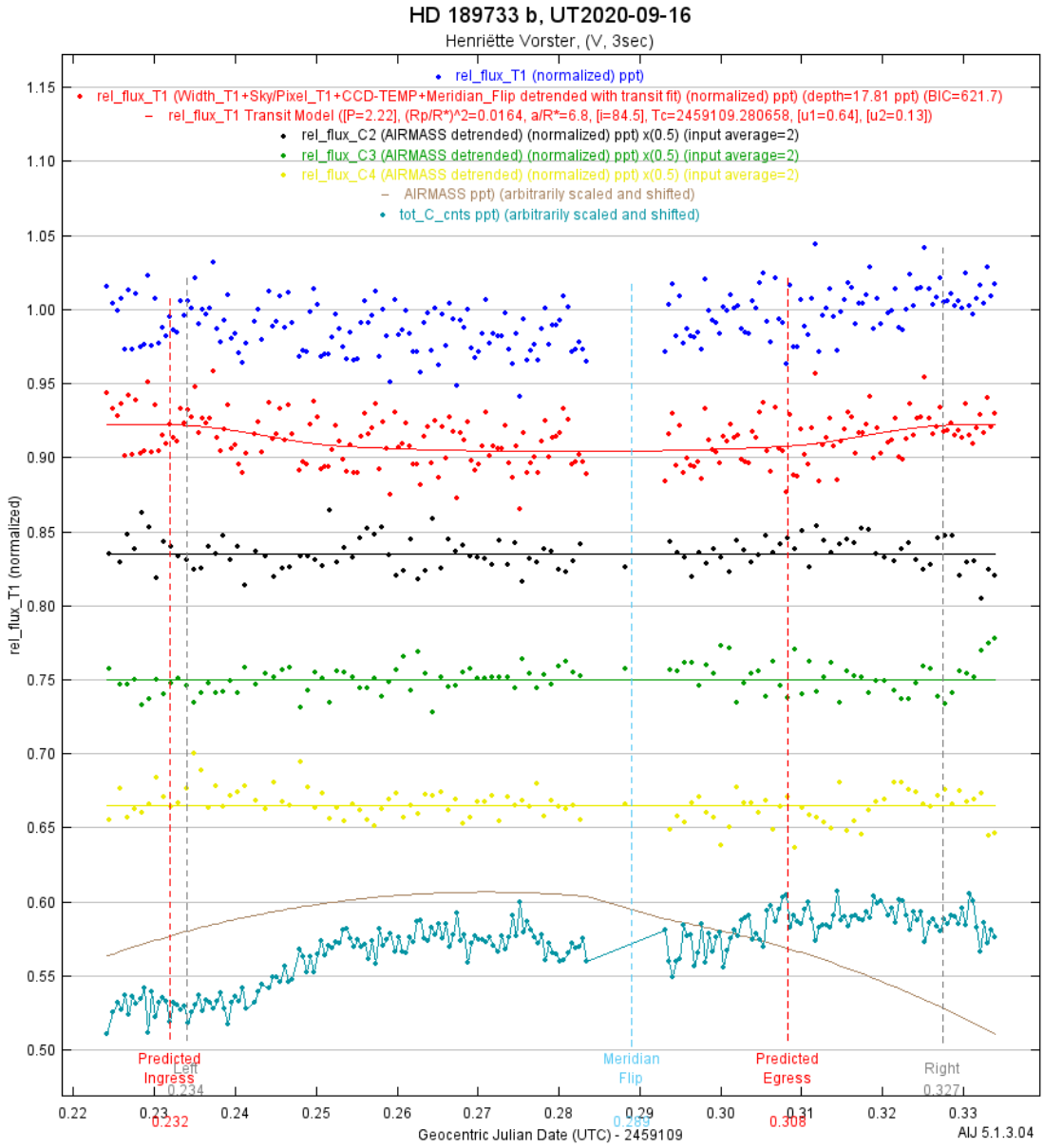

Figure 4.2: HD 189733 b light curve, V-band.

The values extracted from this model are given in table 4.4. As seen in section 2.3.3.3 the inclination and density are dependent on the ratio a/R_* and this ratio is dependent on the duration of the transit. A discrepancy between the values extracted from the model and the values reported by Addison et al. (2019) was thus expected. From the model $a/R_* = 6.8354$ was extracted and Addison et al. (2019) reported the value as $a/R_* = 8.73 \pm 0.15$, this leads to the discrepancy in the values for inclination and density obtained from the model, $i = 84.49$ degrees and $\rho_* = 1.2258$ g/cm^3, versus the reported values, $i = 85.69^{+0.095}_{-0.097}$ degrees and $\rho_* = 2.56 \pm 0.13$ g/cm^3.

The relative flux for the target was still scattered around the transit model and did not track the model, even though the data was normalised and detrended. The depth of the transit in the model was also less than what was expected, and less than what was obtained in the model of the B-band data. The model gave a planet radius of $R_p = 1.0037^{+0.0237}_{-0.0224}$ R_{Jup} while Addison et al. (2019) reported $R_p = 1.119 \pm 0.038$ R_{Jup} and it is thus clear that the B-band model is better than the V-band model.

Properties	Units	Calculated Value	Literature Value
R_p	Radius (R_{Jup})	$1.0037^{+0.0237}_{-0.0224}$	$0.765^{+0.019}_{-0.018}$
i	Inclination (deg)	84.49	$85.69^{+0.095}_{-0.097}$
ρ_*	Density (cgs)	1.2258	2.56 ± 0.13
a/R_*		6.8354	8.73 ± 0.15

Table 4.4: Fit results for HD 189733, V-band (16/09/2020).

R-band Light Curve (08/08/2021)

Figure 4.3 is the light curve for the data obtained on the 8th of August 2021. Due to this observation starting late, it was not possible to capture the start of the transit. AIJ has a feature that allows the selection of either the pre-ingress or post-egress data, or both, for creating the baseline flux mentioned in section 2.3.3.2. In this case only the post-egress data was selected for this purpose and a model fit was applied to the data. The same three comparison stars were selected but were binned with a factor of three for visual purposes.

The irregularity in trend of the total background sky counts is attributed to the high humidity on the night of the observation. The fit was detrended with the airmass; the sky counts for the target star, the Barycentric Julian Date and the meridian flip parameter.

In this model the ingress- and egress-points were respectively 9 and 15 minutes earlier than the predicted points. The model gave $a/R_* = 8.9025$, this is close to what was reported in the literature, $a/R_* = 8.73 \pm 0.15$. Accordingly, the values for $i = 85.77$ degrees and $\rho_* = 2.7082$ g/cm^3, also coincided with the values reported: $i = 85.69^{+0.095}_{-0.097}$ degrees and $\rho_* = 2.56 \pm 0.13$ g/cm^3.

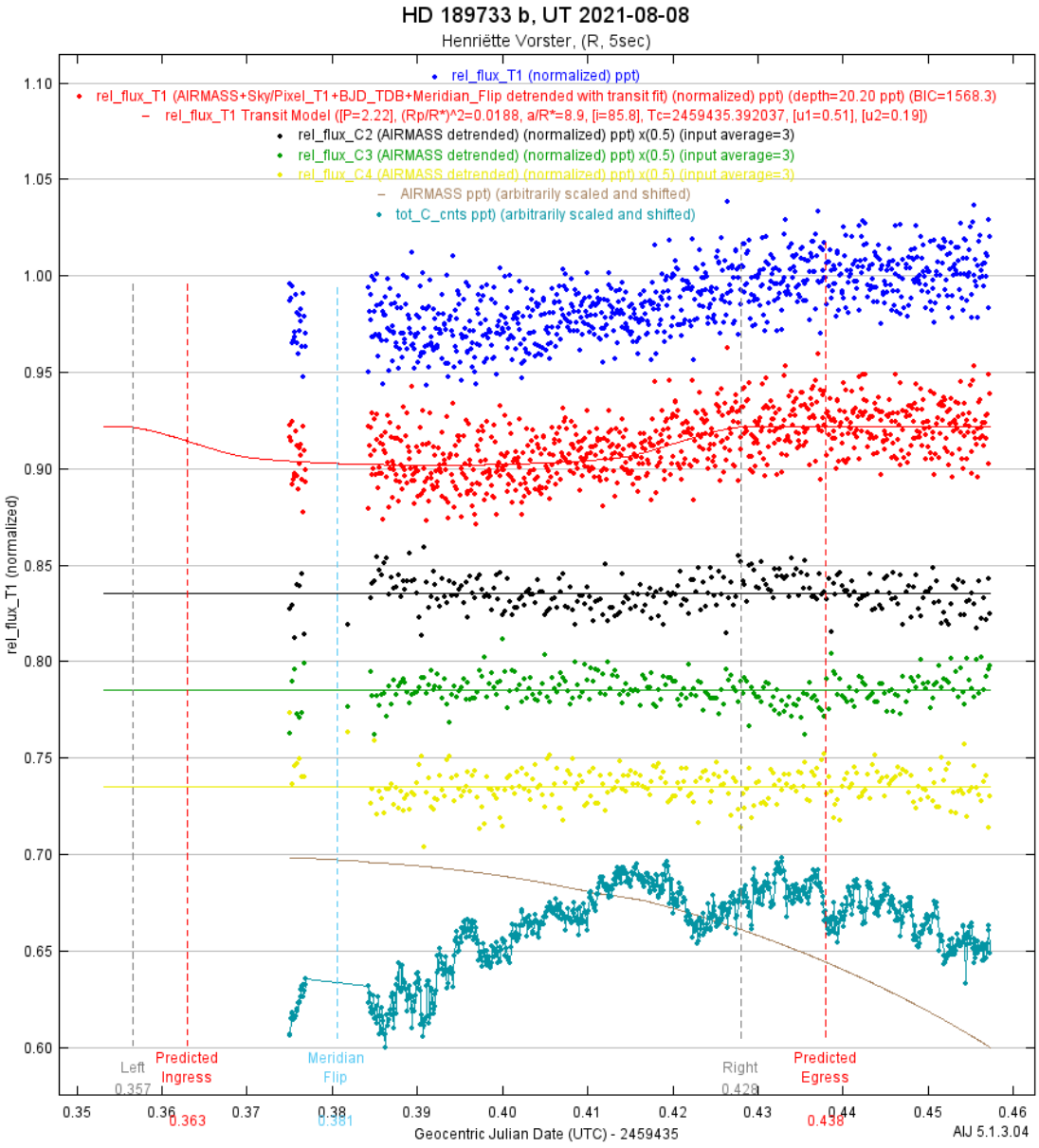

Figure 4.3: HD 189733 b light curve, R-band.

Properties	Units	Calculated Value	Literature Value
R_p	Radius (R_{Jup})	$1.0741^{+0.0254}_{-0.02408}$	$0.765^{+0.019}_{-0.018}$
i	Inclination (deg)	85.77	$85.69^{+0.095}_{-0.097}$
ρ_*	Density (cgs)	2.7082	2.56 ± 0.13
a/R_*		8.9025	8.73 ± 0.15

Table 4.5: Fit results for HD 189733, R-band (08/08/2021).

There was a discrepancy between the planet radius obtained from the model and the reported value. The model calculated the value at $R_p = 1.0741^{+0.0254}_{-0.02408}$ R_{Jup}, compared to

the value found in Addison et al. (2019), $R_p = 1.119 \pm 0.038\ R_{\text{Jup}}$. This discrepancy was attributed to the fact that the transit was not captured completely; and also AIJ's model fitting is not well-suited for modelling half-transits.

B-band Light Curve (07/09/2022)

The light curve for the observation conducted on the 7th of September 2022 is given in figure 4.4. The detrend parameters that were used was the airmass, background sky count for the target, the total background sky counts, the Barycentric Julian Date and the meridian flip. According to the model the duration of the transit was shorter than what was predicted as the ingress- and egress-points were shifted inwards with 5 and 6 minutes, respectively, from the predicted points.

During the course of the observation, the telescope gradually went out of focus; this was noticed most prominently after the meridian flip. This can be seen on the plot for the total background sky count, where the data stopped tracking the airmass curve.

Properties	Units	Calculated Value	Literature Value
R_p	Radius (R_{Jup})	$1.1536^{+0.0272}_{-0.0258}$	$0.765^{+0.019}_{-0.018}$
i	Inclination (deg)	86.06	$85.69^{+0.095}_{-0.097}$
ρ_*	Density (cgs)	3.3290	2.56 ± 0.13
a/R_*		9.5365	8.73 ± 0.15

Table 4.6: Fit results for HD 189733, B-band (07/09/2022).

Table 4.6 lists the values obtained from the model fit. The radius of the planet was calculated as $R_p = 1.1536^{+0.0272}_{-0.0258}\ R_{\text{Jup}}$, which had a small discrepancy with the value reported by Addison et al. (2019), $R_p = 1.119 \pm 0.038\ R_{\text{Jup}}$. The discrepancy between the values of the radius were found to have been caused because the telescope went out of focus as well as the fact that the data points for the detrended relative flux of the target did not follow the same trend after the meridian flip.

From the model $a/R_* = 9.5365$ was retrieved, and since the duration of the transit in the model is shorter, this value does not coincide with the value found in literature, $a/R_* = 8.73 \pm 0.15$. This meant that the values for the inclination and stellar density also did not coincide with the reported values. From the model $i = 86.06$ degrees and the literature reported $i = 85.69^{+0.095}_{-0.097}$ degrees, $\rho_* = 3.3290$ g/cm^3 was also obtained, whilst literature yielded $\rho_* = 2.56 \pm 0.13$ g/cm^3.

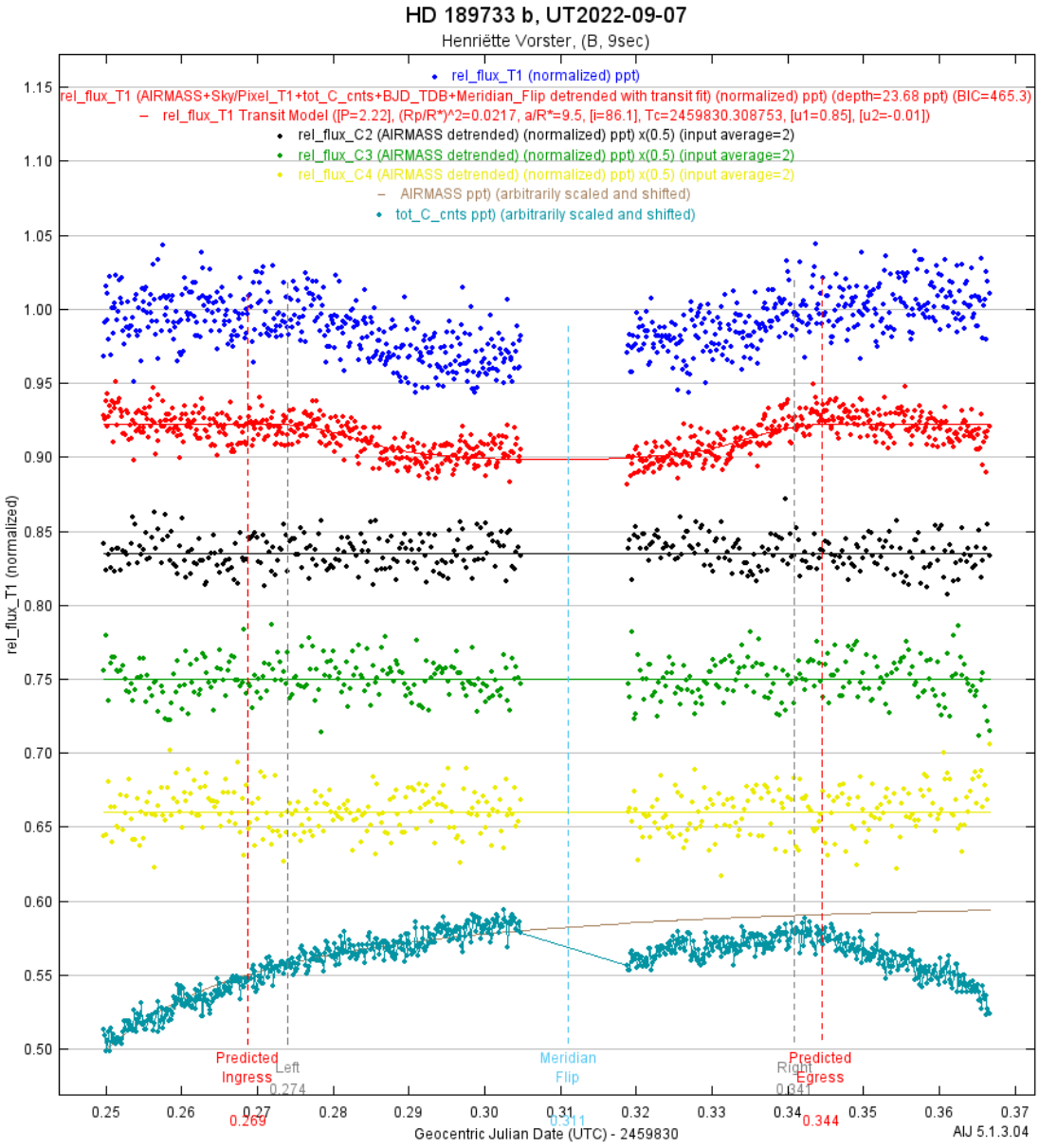

Figure 4.4: HD 189733 b light curve, B-band.

4.2 WASP-7 b

During the observation of WASP-7 the telescope had to be repositioned to ensure that the target did not drift out of the FOV. Due to the repositioning there was only one star present in all the images other than the target star, this meant that only one star could have been selected as a comparison star. The photometry for this target could not be completed to satisfaction; the models that were created from this data are thus unreliable. It was nonetheless decided to continue with the model fit to investigate the effect of selecting only one comparison star. In all the plots for this target there is no light curve for the comparison star since AIJ does not plot the light curve of a comparison star if only one was selected.

The parameters that were used in the creation of the models, along with the system properties, were obtained from Southworth et al. (2011) and Patel and Espinoza (2022), and are listed in table 4.7. Southworth et al. (2011) did not determine the impact parameter or the orbital period, but Patel and Espinoza (2022) based their work off of that done by Southworth et al. (2011) and the values for those variables were obtained from Patel and Espinoza (2022).

Parameter	Units	Value	Reference
P	Period (days)	4.9546417	Patel and Espinoza (2022)
R_*	Radius ($R_\odot$)	1.432 ± 0.092	Southworth et al. (2011)
b		0.530	Patel and Espinoza (2022)
System properties			
R_p	Radius (R_{Jup})	1.330 ± 0.093	Southworth et al. (2011)
i	Inclination (deg)	87.03 ± 0.93	Southworth et al. (2011)
ρ_*	Density (cgs)	0.611 ± 0.104	Southworth et al. (2011)
a/R_*		$9.074^{+0.532}_{-0.476}$	Southworth et al. (2011)

Table 4.7: Values for WASP-7 parameters and system properties

Figure 4.5 shows the light curves for the B- and I-bands. The data for the B-band was detrended with the following parameters: the airmass, the position of the star on the x-axis and the total background sky counts. For the V-band data the detrend parameters that were used were: the airmass, the change in the point-spread function of the target, the background sky count for the target and the total background sky counts.

The models for the two filters are vastly different; the transit depth of the B-band model is much larger than the depth of the I-band model, which will lead to a large difference in the radii extracted from the models. Table 4.8 lists the values that were calculated from these models. For the B-band, the model obtained $R_p = 2.1996 \pm 0.1413\ R_{\text{Jup}}$ and for the I-band, the model obtained $R_p = 0.9936 \pm 0.0638\ R_{\text{Jup}}$. Comparing the total background sky counts between the B- and I-band plots, it was seen that the I-band data is more sporadic and does not track the airmass curve as well as on the B-band plot. This might be a reason why there is such a large discrepancy between the two models. The reported value of the radius of the exoplanet is $R_p = 1.330 \pm 0.093\ R_{\text{Jup}}$, the values obtained from the models differ significantly from this value. This is simply because of the poor photometry since only one comparison star was used.

The duration of the transit according to the model for the B-band data, figure 4.5a, is not far off from the predicted duration. The egress-point of the model is the same as the predicted egress point, but the ingress-point is a bit earlier than what was predicted. The model reflected a value of $a/R_* = 10.0698$, whilst the reported value was: $a/R_* = 9.074^{+0.532}_{-0.476}$. This led to an inconsistency in the inclination angle ($i = 86.98$ degrees) and

stellar density ($\rho_* = 0.7861\ g/cm^3$) of the model compared to that recorded by Southworth et al. (2011), $i = 87.03 \pm 0.93$ degrees and $\rho_* = 0.611 \pm 0.104$ g/cm^3.

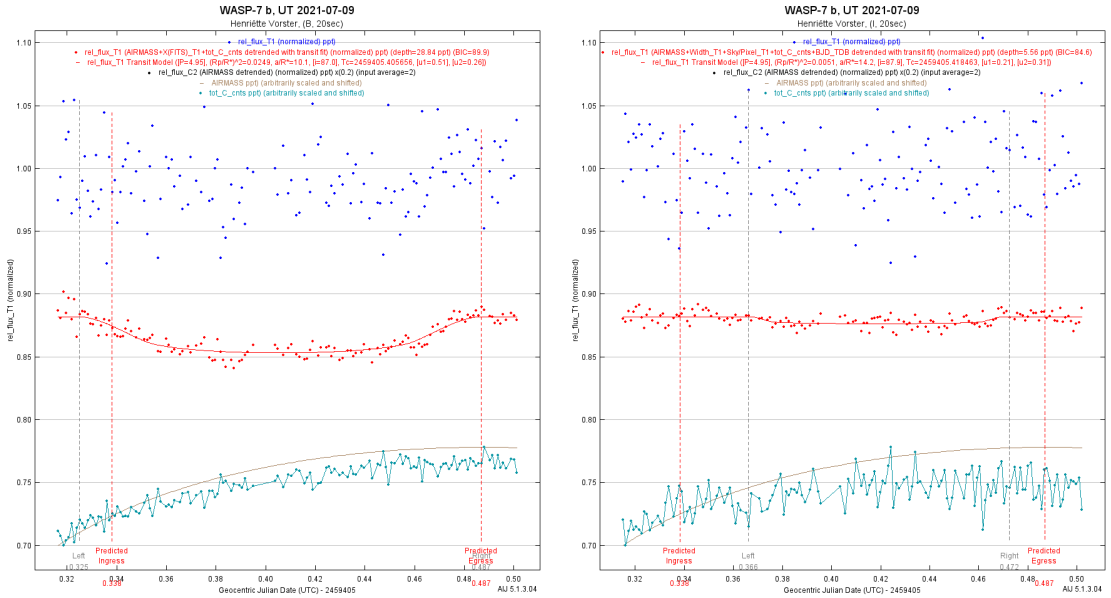

(a) B-band (b) I-band

Figure 4.5: Light curves for WASP-7 b

For the I-band model, figure 4.5b, the duration of the transit and the predicted ingress- and egress-points were completely inconsistent with the predicted values. The ratio a/R_* was extracted from the model as 14.2647 and Southworth et al. (2011) reported it to be $a/R_* = 9.074^{+0.532}_{-0.476}$. The stellar density obtained from the model was $\rho_* = 2.2263$ g/cm^3 and it was reported to be $\rho_* = 0.611 \pm 0.104$ g/cm^3, this large discrepancy was due the ratio a/R_* being cubed in equation 2.5 with which the density is calculated. The inclination angle extracted from the model, $i = 87.87$ degrees, shows a small discrepancy from the literature, $i = 87.03 \pm 0.93$ degrees.

Properties	Units	B-band	I-band	Literature Value
R_p	Radius (R_{Jup})	2.1996 ± 0.1413	0.9936 ± 0.0638	1.330 ± 0.093
i	Inclination (deg)	86.98	87.87	87.03 ± 0.93
ρ_*	Density (cgs)	0.7861	2.2263	0.611 ± 0.104
a/R_*		10.0698	14.2647	$9.074^{+0.532}_{-0.476}$

Table 4.8: Fit results for WASP-7 b, B- and I-band.

As can be seen from figure 4.5, by selecting only one comparison star there is a large discrepancy between the models for different filters. The I-band plot showed an irregular trend in the total background sky counts, from which it was concluded that for different targets it would be more advantageous to use certain filters for these types of observations.

Due to insufficient photometry, the results obtained were undependable; the repositioning of the telescope also contributed to the unreliable results.

In figure 4.6 the light curves for the V- and R-bands are shown. In both light curves, just after the modelled ingress-point, the data points are scattered and do not follow the trend of the out-of-transit data points. These are the data points that were extracted from the images just after the telescope was repositioned to prevent the target from drifting out of the FOV. Since AIJ modelled these outliers as the transit event, these models are inconclusive. A comparison cannot be made between the values found in literature and the values extracted from the models, since the models were not reliable.

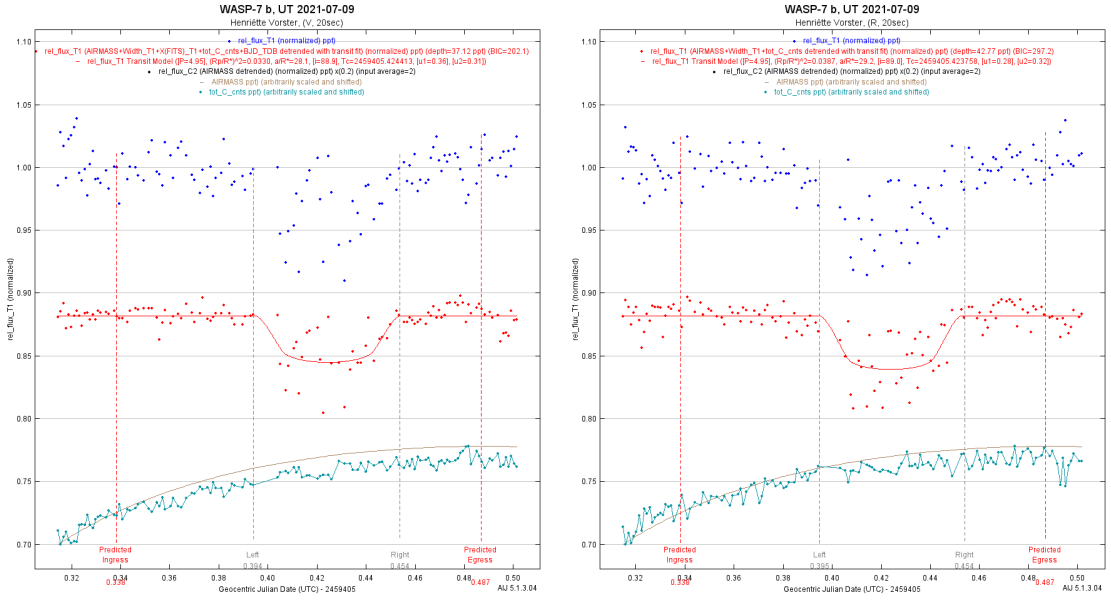

(a) V-band (b) R-band

Figure 4.6: Light curves for WASP-7 b

4.3 WASP-74 b

As discussed in section 3.4 the telescope went out of focus during the observation of this target. Figure 4.7 shows the light curves for the V- and I-band data. In the middle of the light curve, some of the data points are unmistakable outliers, these data points are from the images that were taken just after the telescope was focused. Due to the size difference of the stars in the unfocused images versus the focused images (see figure 3.1), the aperture size during photometry was too big for the stars in the focused images; this is the reason for the outliers. In the other data sets where there was a problem with the telescope going out of focus, the focus gradually worsened throughout the observation. With this observation, on the other hand the focus abruptly shifted from one image to the next.

Parameter	Units	Value	Reference
P	Period (days)	2.137750 ± 0.000001	Hellier et al. (2015)
R_*	Radius ($R_\odot$)	1.64 ± 0.05	Hellier et al. (2015)
b		0.860 ± 0.006	Hellier et al. (2015)
System properties			
R_p	Radius ($R_{\rm Jup}$)	1.56 ± 0.06	Hellier et al. (2015)
i	Inclination (deg)	79.81 ± 0.24	Hellier et al. (2015)
ρ_*	Density (cgs)	0.476 ± 0.025	Hellier et al. (2015)

Table 4.9: Values for WASP-74 parameters and system properties

For the two plots shown in figure 4.7 no detrend parameters, except for airmass, were applied. Since AIJ recognises the outliers as the transit event, no model fit applied to these data sets will yield an acceptable model. These data points were removed from the data sets and the photometry and model fit were performed again. Considering that the outliers were present in the data for both the B-band and the I-band, but not as discernibly (figures 4.10 and 4.12), it was thus decided to redo the photometry for those filters as well. The parameters used in these models and the system properties are listed in table 4.9.

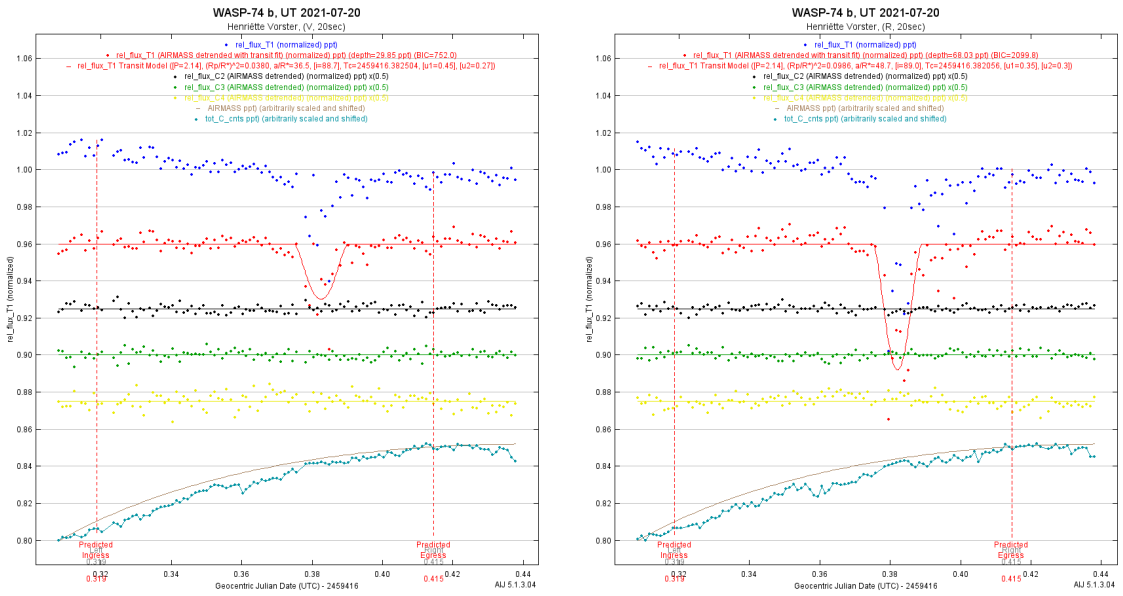

Figure 4.7: WASP-74 b V-band and I-band light curves with outlier data.

V-band light curve

The plot given in figure 4.8 shows the light curve for the V-band after the outlier data was removed. The data for the target star was detrended with only the Barycentric Julian Date as there is a large gap in the data. A much more accurate model was obtained after the outliers were removed. The ingress-point according to the model, was 6 minutes after

the predicted point and the egress-point yielded from the model was 15 minutes after the predicted point.

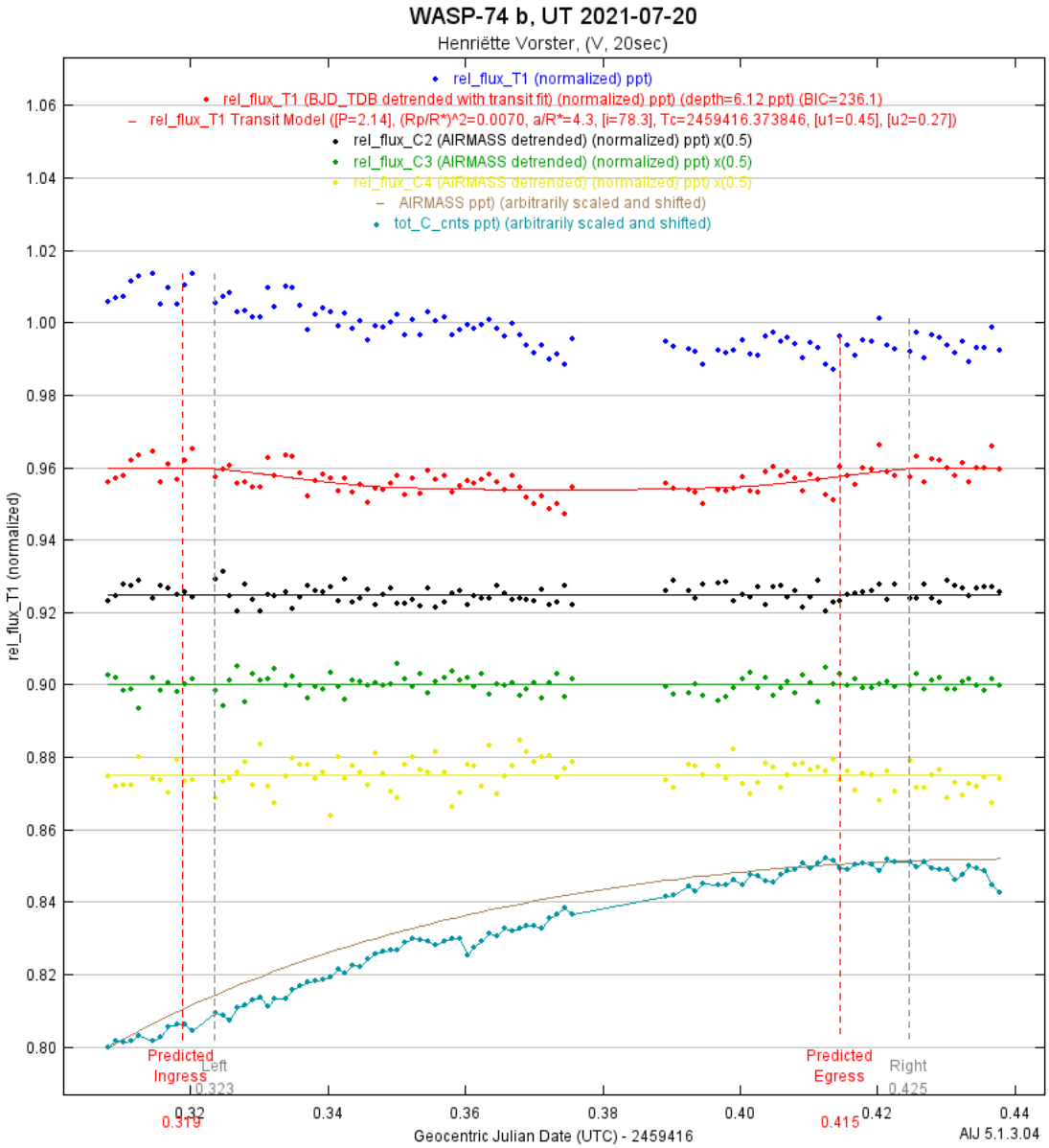

Figure 4.8: WASP-74 b light curve without outlier data, V-band.

The retrieved value of $a/R_* = 4.2583$ yields an inclination angle of $i = 78.35$ degrees and stellar density of $\rho_* = 0.3193$ g/cm^3, which does not correlate very well with the values reported by Hellier et al. (2015): $i = 79.81 \pm 0.24$ degrees and $\rho_* = 0.476 \pm 0.025$ g/cm^3. The reason for this discrepancy was that the model's transit duration was longer than what was predicted, and both equation 2.3 and 2.5 are dependent on the ratio a/R_* whilst this in turn is dependent on the duration of the transit (equation 2.4).

The exoplanet radius extracted from the model was $R_p = 1.3316 \pm 0.0406\ R_{\text{Jup}}$, whilst the reported value was $R_p = 1.56 \pm 0.06\ R_{\text{Jup}}$. There is a substantial discrepancy between these

values due to various possible reasons, the effect of focusing the telescope mid-observation might have impacted the data more severely than initially thought or the removal of the data points left a too large gap in the data for the model fit to be accurate.

Properties	Units	Calculated Value	Literature Value
R_p	Radius (R_{Jup})	1.3316 ± 0.0406	1.56 ± 0.06
i	Inclination (deg)	78.35	79.81 ± 0.24
ρ_*	Density (cgs)	0.3193	0.476 ± 0.025
a/R_*		4.2583	

Table 4.10: Fit results for WASP-74, V-band.

R-band light curve

Figure 4.9 shows the light curve that was obtained for the R-band after the outlier data was removed. The data for this transit event was detrended with the measurement of change in the point-spread function of the target, the shift of the target on the Y-axis and the total background sky counts. According to the model both the predicted ingress- and egress-points are within a minute from the predicted points, thus the duration of the transit, as per the model, is only 2 minutes shorter than what was predicted.

The system properties from the model are given in table 4.11. The reported value of $R_p = 1.56 \pm 0.06\ R_{\text{Jup}}$ does not correlate with the value of $R_p = 1.3815 \pm 0.0421\ R_{\text{Jup}}$. It is possible that this was due to the removal of the data points and the large change in the images after the telescope was refocused.

The same is not true for the other system properties, the model yielded $i = 79.64$ degrees whilst the reported value was $i = 79.81 \pm 0.24$ degrees and $\rho_* = 0.4523$ g/cm^3 was extracted, with the reported value being $\rho_* = 0.476 \pm 0.025$ g/cm^3. Since the model's transit duration is so close to the predicted duration, these values were consistent with the reported values. The removal of the outlier data yielded a better model with the values for the inclination angle and stellar density being close to what was reported in Hellier et al. (2015), as can be seen from the results for both the V- and B-band light curves.

Properties	Units	Calculated Value	Literature Value
R_p	Radius (R_{Jup})	1.3815 ± 0.0421	1.56 ± 0.06
i	Inclination (deg)	79.64	79.81 ± 0.24
ρ_*	Density (cgs)	0.4523	0.476 ± 0.025
a/R_*		4.7821	

Table 4.11: Fit results for WASP-74, R-band.

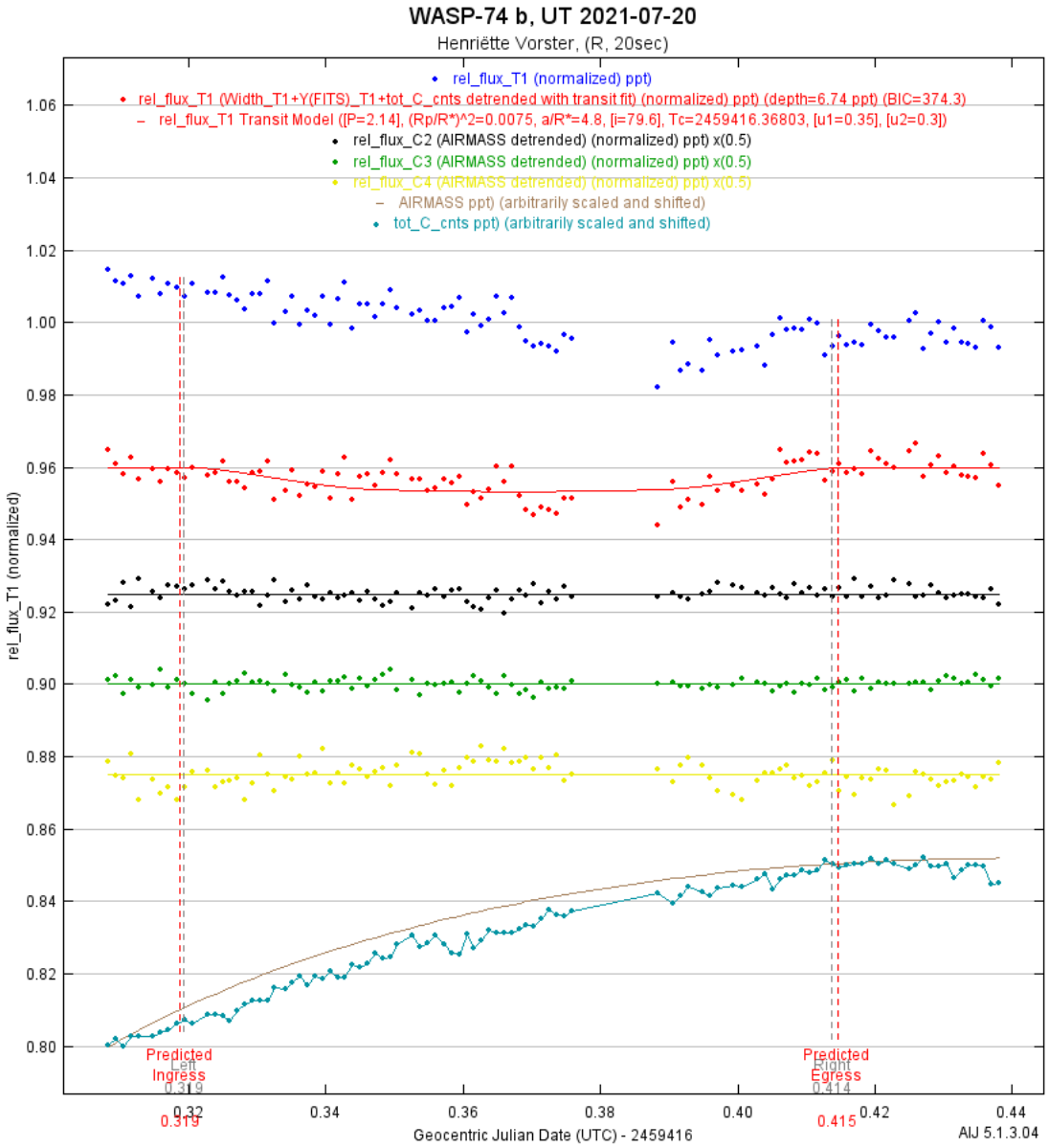

Figure 4.9: WASP-74 b light curve without outlier data, R-band.

B-band light curves

Figure 4.10 shows the light curve obtained for the B-band without removing the outlier data. The detrend parameters used during the model fit were: the airmass, the background sky counts for the target star and the total background sky counts. The duration of the transit according to the model is a bit longer than what was predicted, the ingress-point as per the model is 3 minutes after the predicted ingress-point and the egress-point was 9 minutes after the predicted point of egress. The reason for this difference was the quality of the data, which was tainted after refocusing the telescope.

The inclination angle and stellar density obtained from the model was: $i = 78.58$ degrees and $\rho_* = 0.3391$ g/cm^3, this showed a discrepancy when compared to the values of the properties reported in Hellier et al. (2015): $i = 79.81 \pm 0.24$ degrees and $\rho_* = 0.476 \pm$

0.025 g/cm^3. The reason for the discrepancy was that the duration of the transit of the model is inconsistent with the predicted duration, and the inclination angle and density is dependent on the duration of the transit.

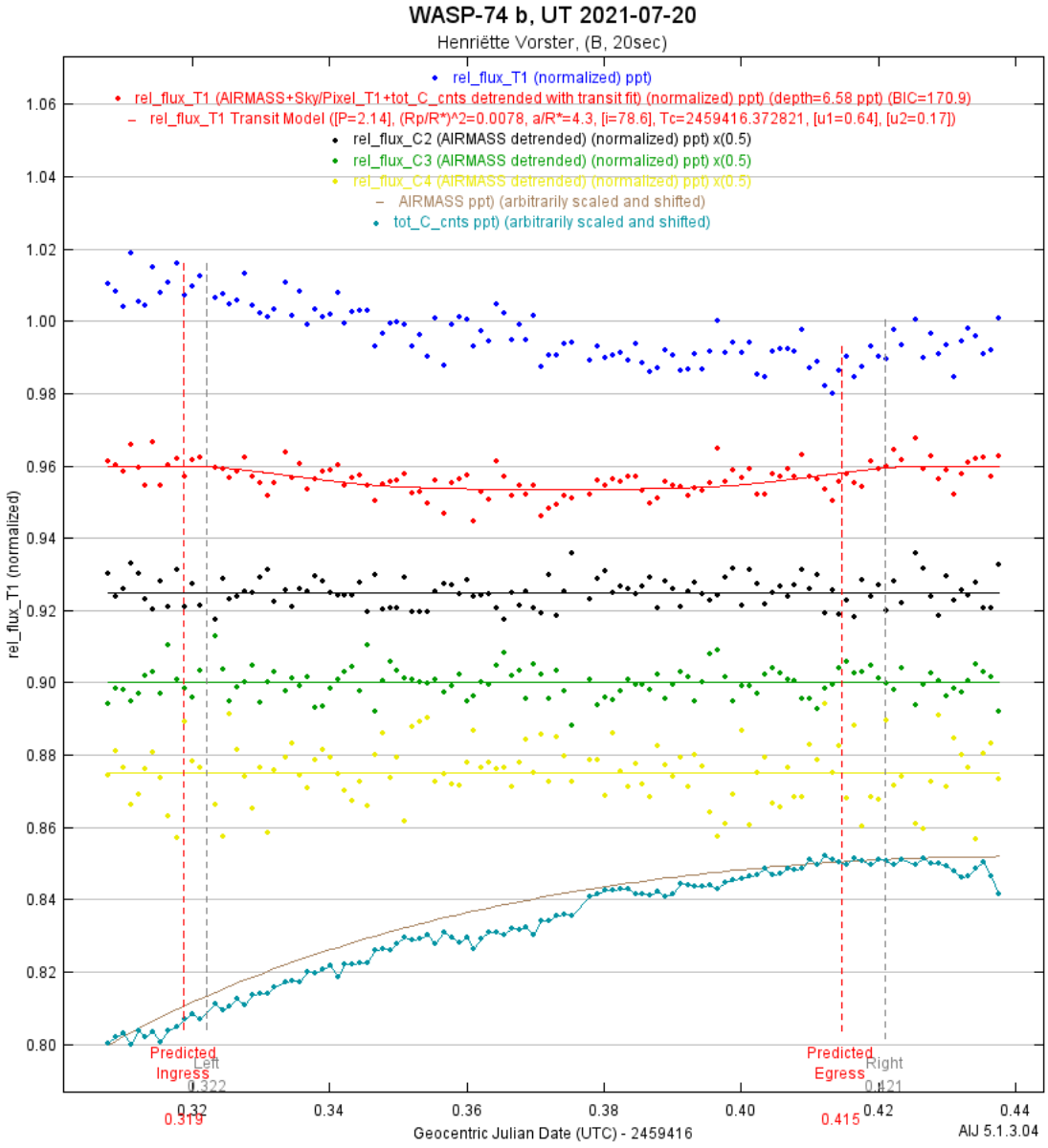

Figure 4.10: WASP-74 b light curve, B-band.

The model obtained from the B-band data with the outliers removed is given in figure 4.11. The data was detrended with the airmass, the background sky counts for the target star and the total background sky counts. The ingress- and egress-points of this model are respectively, 23 minutes after and 11 minutes before the predicted points. This meant that the duration of the modelled transit is 34 minutes shorter than what was predicted.

Since this model showed a large discrepancy with the predicted duration of the transit, the inclination angle and stellar density extracted from the model, $i = 81.79$ degrees

and $\rho_* = 0.9048$ g/cm^3, did not coincide with the reported values at all. Hellier et al. (2015) reported the inclination angle to be $i = 79.81 \pm 0.24$ degrees and the stellar density $\rho_* = 0.476 \pm 0.025$ g/cm^3.

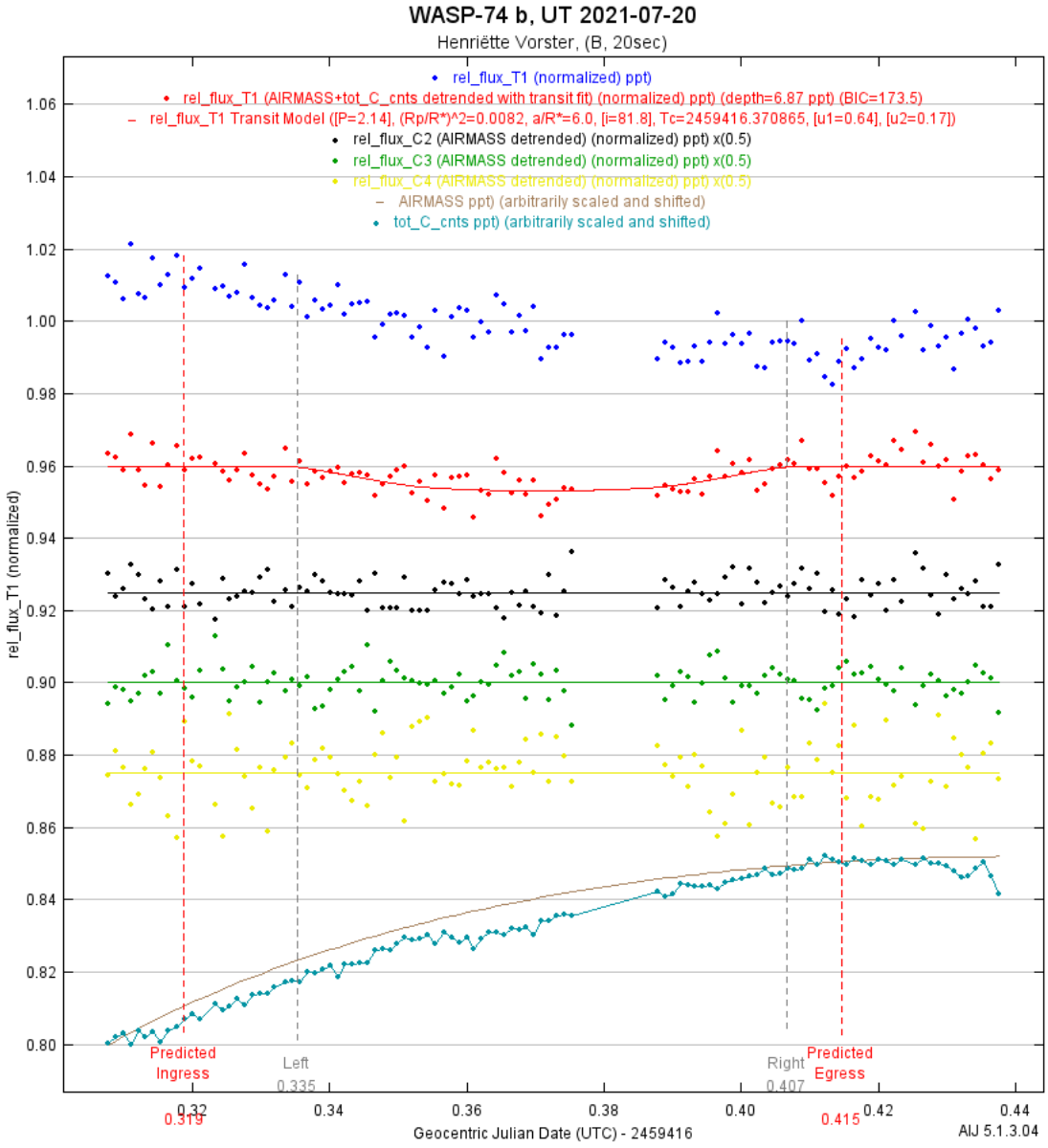

Figure 4.11: WASP-74 b light curve without outlier data, B-band.

The radius of the exoplanet extracted from the model with the outlier data, $R_p = 1.4129 \pm 0.0431$ R_{Jup}, coincides with the value from the model without the outlier data, $R_p = 1.4441 \pm 0.0440$ R_{Jup}, but there was a discrepancy between these two values and the reported value of $R_p = 1.56 \pm 0.06$ R_{Jup}. Apparently removing the outlier data improved the models, but not enough to coincide with literature. The properties of the system extracted from both models of the B-band data are listed in table 4.12.

Properties	Units	With outlier	Without outlier	Literature Value
R_p	Radius (R_{Jup})	1.4129 ± 0.0431	1.4441 ± 0.0440	1.56 ± 0.06
i	Inclination (deg)	78.58	81.79	79.81 ± 0.24
ρ_*	Density (cgs)	0.3391	0.9048	0.476 ± 0.025
a/R_*		4.3442	6.0257	

Table 4.12: Fit results for WASP-74 b, B-band.

I-band light curves

Figure 4.12 was the light curve model obtained from the I-band data where the outlier data was included. The flux of the target star was detrended with the following parameters: the shift of the target on both the X- and Y-axes and the background sky counts for the target. The transit event according to the model, transpired about 5 minutes before the predicted event and the duration of the transit is only a minute shorter than what was predicted.

The system properties extracted from this model are given in table 4.13. The value retrieved for the inclination angle, $i = 80.00$ degrees, coincides with the range of the value reported by Hellier et al. (2015), $i = 79.81 \pm 0.24$ degrees. The value retrieved for the stellar density, $\rho_* = 0.5023$ g/cm^3, is also in close proximity to the reported value, $\rho_* = 0.476 \pm 0.025$ g/cm^3. The aforementioned is due to the fact that the transit duration from the model is very close to the predicted duration.

The model that was obtained from the data which excluded the outliers is given in figure 4.13; the data was detrended with the same parameters as the previous model that included the outlier data. The models had the same ingress-point, but the model without the outlier data has an egress point that was 11 minutes before the predicted egress-point. The transit duration of the model was thus approximately 10 minutes shorter than what was predicted.

Table 4.13 lists the system properties obtained from the model. The inclination angle and stellar density extracted from the model corresponds more closely with the reported values than the model including the outlier data. The inclination angle: $i = 79.81 \pm 0.24$ degrees, was extracted from the model, whilst the reported value was $i = 79.81 \pm 0.24$ degrees. For the stellar density $\rho_* = 0.4895$ g/cm^3 was obtained, whilst the reported value was $\rho_* = 0.476 \pm 0.025$ g/cm^3.

Properties	Units	With outlier	Without outlier	Literature Value
R_p	Radius (R_{Jup})	1.5815 ± 0.0482	1.3649 ± 0.0416	1.56 ± 0.06
i	Inclination (deg)	80.00	79.91	79.81 ± 0.24
ρ_*	Density (cgs)	0.5023	0.4895	0.476 ± 0.025
a/R_*		4.9521	4.9097	

Table 4.13: Fit results for WASP-74 b, I-band.

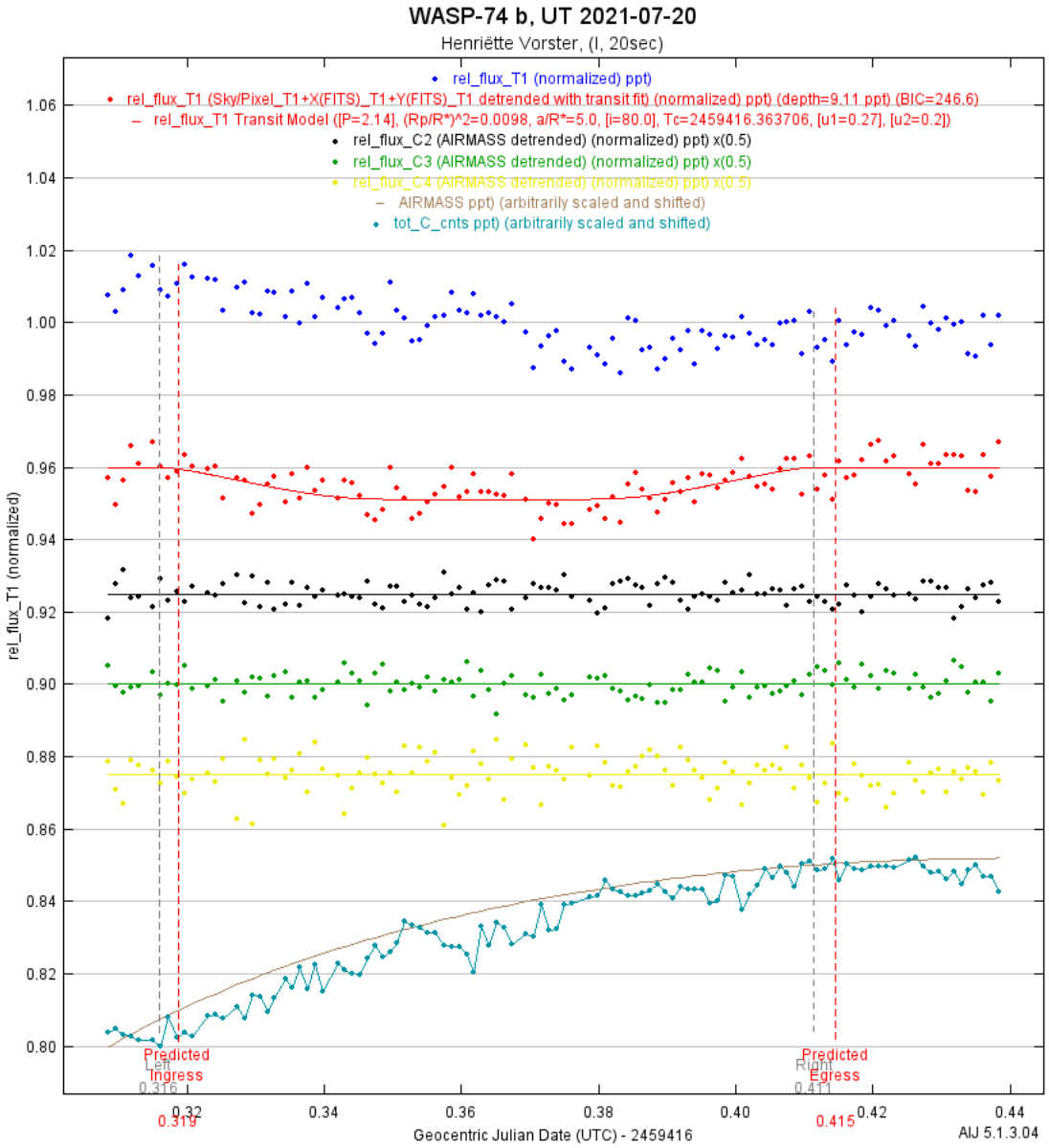

Figure 4.12: WASP-74 b light curve, I-band.

The radii obtained from the created models do not coincide with each other. For the model including outlier data, $R_p = 1.5815 \pm 0.0482\ R_{\text{Jup}}$ was extracted and for the model excluding the outlier data $R_p = 1.3649 \pm 0.0416\ R_{\text{Jup}}$ was obtained. Whilst comparing these values to the reported value of $R_p = 1.56 \pm 0.06\ R_{\text{Jup}}$, it is clear that the model including the outlier data coincides better with the reported value.

In the instance of the I-band, the model with the outlier data modelled the depth of the transit better, but the model without the outlier data presented a better fit in regard to the inclination angle and the stellar density. From the aforementioned, it was assumed that the outlier data would not have as large an effect on the model fit as initially predicted, but by removing the data, more accurate values were obtained for the inclination angle and stellar density.

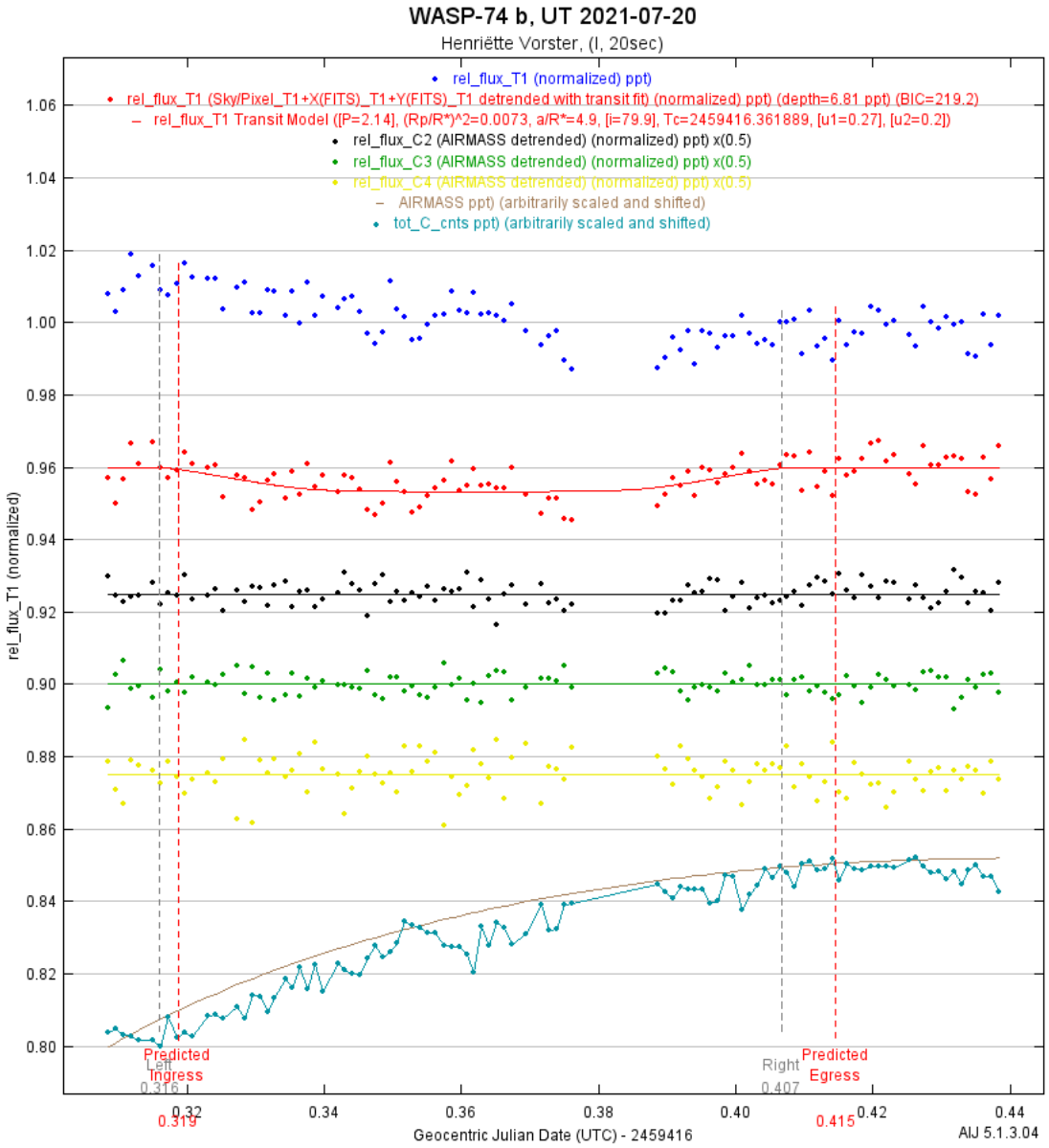

Figure 4.13: WASP-74 b light curve without outlier data, I-band.

4.4 HAT-P-57 b

Since the observation started late, the ingress-point of this target was not fully captured. The data after the predicted egress-point was used to create a baseline flux for this model. The parameters that were used in the creation of the models for this target are given in table 4.14, which also list the system properties.

The humidity on the day of this observation was very high at about 48% and thus an abnormal trend in the total background sky counts was expected. Only two stars were viable to use as comparison stars during the photometry phase; their light curves were binned with a factor of two on the plots given below.

Parameter	Units	Value	Reference
P	Period (days)	2.4652950 ± 0.0000032	Hartman et al. (2015)
R_*	Radius ($R_\odot$)	1.500 ± 0.050	Hartman et al. (2015)
b		$0.177^{+0.090}_{-0.084}$	Hartman et al. (2015)
System properties			
R_p	Radius ($R_{\rm Jup}$)	1.413 ± 0.054	Hartman et al. (2015)
i	Inclination (deg)	88.26 ± 0.85	Hartman et al. (2015)
ρ_*	Density (cgs)	$0.615^{+0.022}_{-0.036}$	Hartman et al. (2015)
a/R_*		$5.825^{+0.069}_{-0.116}$	Hartman et al. (2015)

Table 4.14: Values for HAT-P-57 parameter and system properties

B-band Light Curve

For this model, figure 4.14, the detrend parameters that were used was the measure of the drift of the target on both the X- and Y-axes. The egress-point, according to the obtained model, was 7 minutes before the predicted point and the ingress-point of the model, was 20 minutes before the predicted ingress-point. It is presumed that this was due to an insufficient amount of data before the predicted ingress-point of the transit and also because AIJ is not well-suited to model half-transits. The aforementioned would also lead to a discrepancy in the values for the inclination angle and stellar density calculated from the model, when compared to the values found in literature.

Properties	Units	Calculated Value	Literature Value
R_p	Radius ($R_{\rm Jup}$)	1.3502 ± 0.4559	1.413 ± 0.054
i	Inclination (deg)	88.14	88.26 ± 0.85
ρ_*	Density (cgs)	0.5001	$0.615^{+0.022}_{-0.036}$
a/R_*		5.4382	$5.825^{+0.069}_{-0.116}$

Table 4.15: Fit results for HAT-P-57 b, B-band.

The values for the system-properties extracted from the model are listed in table 4.15. $R_p = 1.3502 \pm 0.4559\ R_{\rm Jup}$ was extracted from the model, which reflects a small discrepancy with the reported value of $1.413 \pm 0.054\ R_{\rm Jup}$, where the calculated errors in the values overlap. The reason for the discrepancy was because the baseline flux could only be calculated from the post-transit data points.

The value of $a/R_* = 5.4382$ was extracted from the model, and from Hartman et al. (2015) the value was reported to be $a/R_* = 5.825^{+0.069}_{-0.116}$, the value obtained does not coincide with the reported value. The duration of the transit differs with 13 minutes from the predicted duration. This could be partly due to the time deficiency of the computer at Nooitgedacht,

but also the insufficient data before the predicted start time of the transit. The values that depend on this ratio were extracted from the model as: $i = 88.14$ degrees and $\rho_* = 5.4382$ g/cm^3. The inclination angle coincides with the reported value of $i = 88.26 \pm 0.85$ degrees, but the stellar density showed a larger deviation from the value $\rho_* = 0.615^{+0.022}_{-0.036}$ g/cm^3. The deviation stems from equation 2.5, where the ratio a/R_* is cubed.

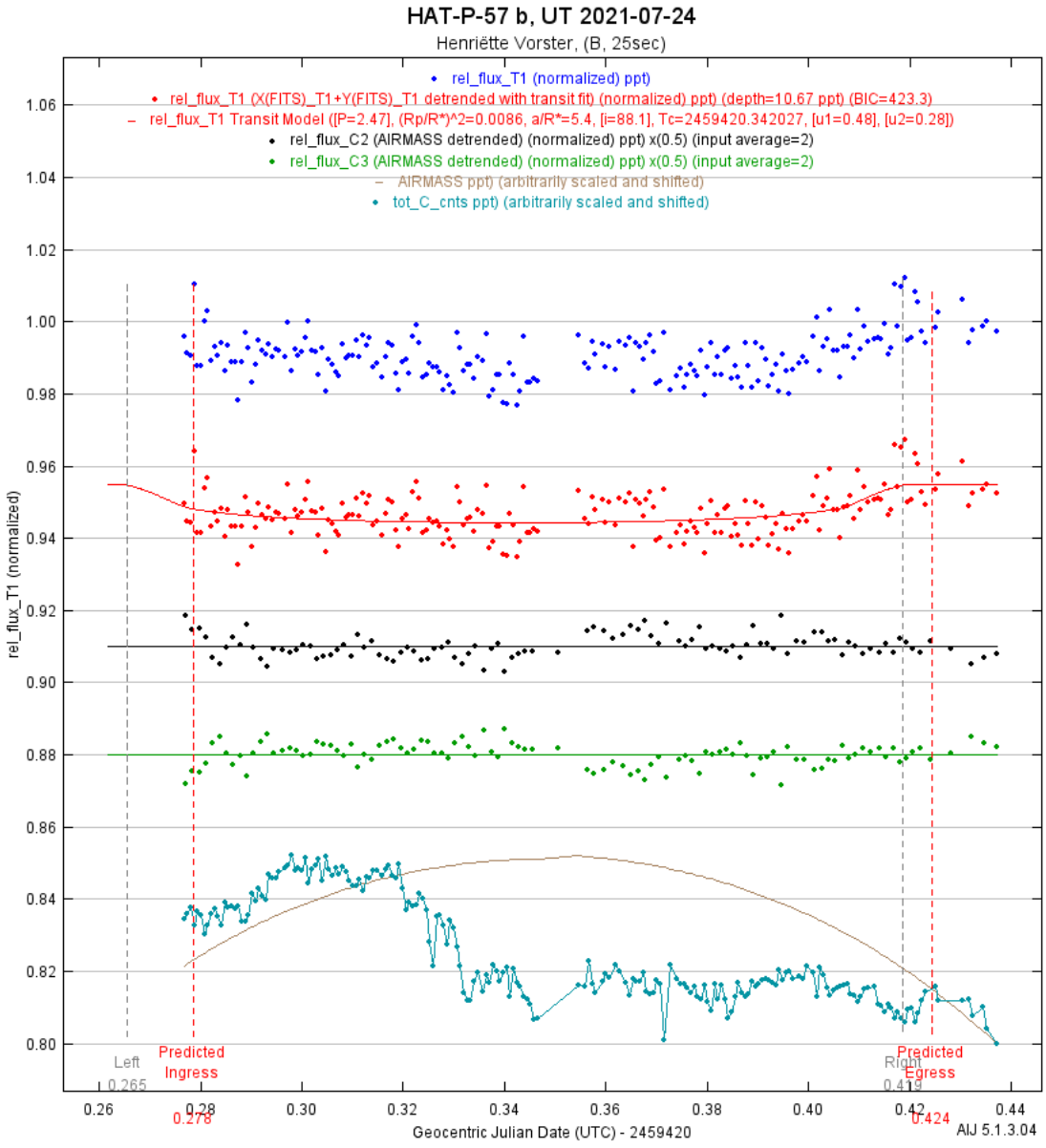

Figure 4.14: HAT-P-57 b light curve, B-band.

V-band Light Curve

For this model, figure 4.15, the data was detrended with the total background sky counts for the target and the parameter for the shift of the target on the Y-axis. The duration of the transit according to the model, is the same as the predicted duration, but the ingress-

and egress-points according to the model is 11 minutes earlier.

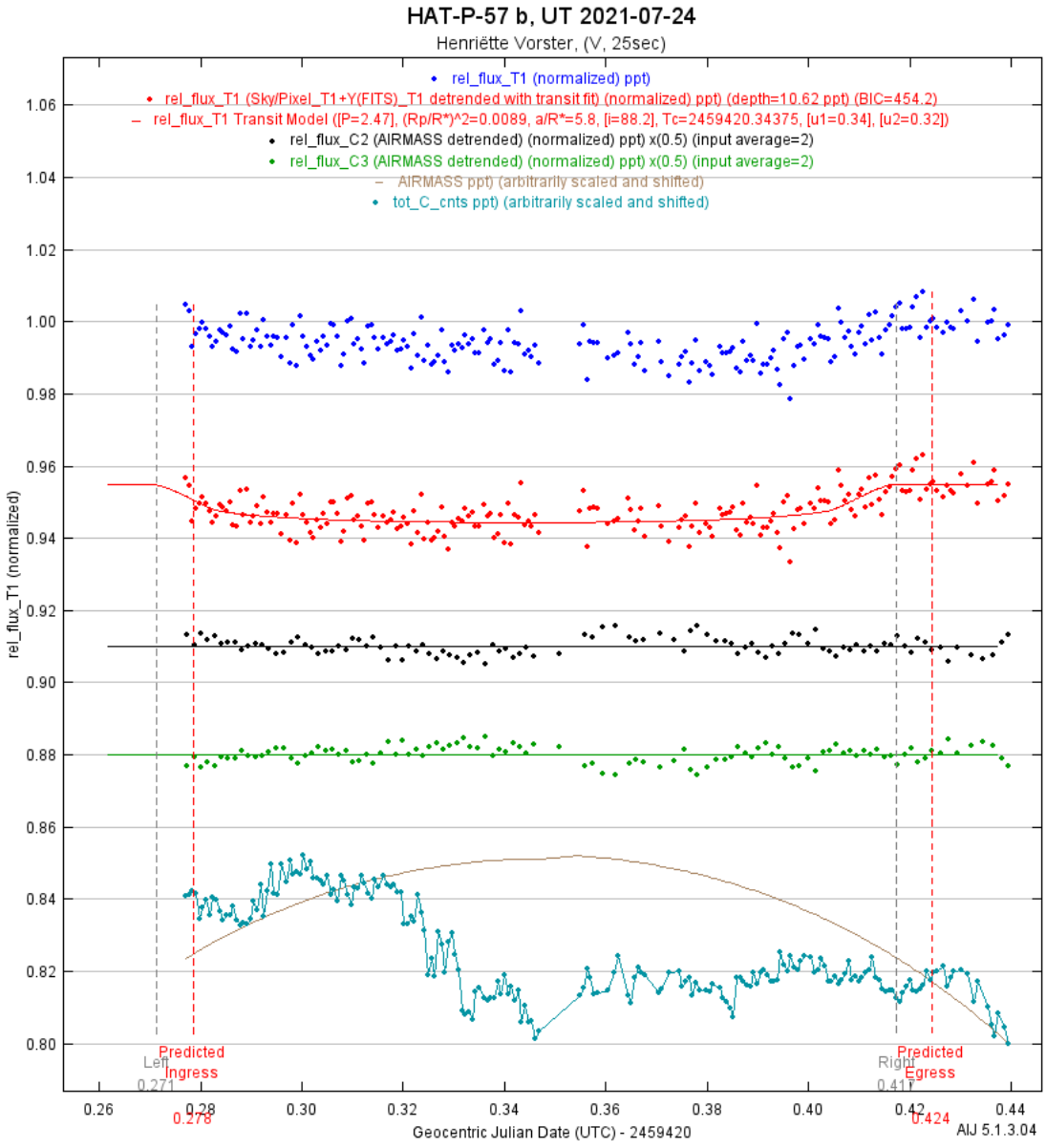

Figure 4.15: HAT-P-57 b light curve, V-band.

The radius of the exoplanet extracted from the model was $R_p = 1.3781 \pm 0.0459\ R_{\text{Jup}}$, which was close in range to the value of $R_p = 1.413 \pm 0.054\ R_{\text{Jup}}$ obtained from literature. The ratio a/R_* was reported to be $5.825^{+0.069}_{-0.116}$ and a value in close proximity to this: $a/R_* = 5.7783$ was extracted from the model. This led to the values, $i = 88.24$ degrees and $\rho_* = 0.6000$ g/cm^3 coinciding extremely well with the reported values: $i = 88.26 \pm 0.85$ degrees and $\rho_* = 0.615^{+0.022}_{-0.036}$ g/cm^3. This was a very accurate model despite the challenges experienced with the observation.

Properties	Units	Calculated Value	Literature Value
R_p	Radius ($R_{\rm Jup}$)	1.3781 ± 0.0459	1.413 ± 0.054
i	Inclination (deg)	88.24	88.26 ± 0.85
ρ_*	Density (cgs)	0.6000	$0.615^{+0.022}_{-0.036}$
a/R_*		5.7783	$5.825^{+0.069}_{-0.116}$

Table 4.16: Fit results for HAT-P-57 b, V-band.

4.5 WASP-80 b

This system has one of the largest transit depths that have been recorded so far (Triaud et al., 2013). This is also the system for which the best results were obtained. Figure 4.16 shows the light curve obtained for the transit event and table 4.17 gives the parameters used in the creation of the model. Three comparison stars were used and their data points were binned with a factor of 2. The detrend parameters used in the creation of the model included: the change in the point-spread function of the target star and the total background sky counts.

Parameter	Units	Value	Reference
P	Period (days)	$3.06785234^{+0.00000083}_{-0.00000079}$	Triaud et al. (2015)
R_*	Radius ($R_\odot$)	$0.586^{+0.017}_{-0.018}$	Triaud et al. (2015)
b		$0.215^{+0.020}_{-0.022}$	Triaud et al. (2015)
System properties			
R_p	Radius ($R_{\rm Jup}$)	$0.9990^{+0.0300}_{-0.0310}$	Triaud et al. (2015)
i	Inclination (deg)	$89.02^{+0.11}_{-0.10}$	Triaud et al. (2015)
ρ_*	Density (cgs)	$4.050^{+0.077}_{-0.121}$	Triaud et al. (2015)
a/R_*		$12.63^{+0.08}_{-0.13}$	Triaud et al. (2015)

Table 4.17: Values for WASP-80 parameter and system properties

The ingress- and egress-points according to the model is the same as the predicted points. The total background sky counts, at the bottom of the plot, shows a deviation that start about halfway through the observation, the reason for this trend is that the focus of the telescope started to shift. Towards the end of the observation the focus of the telescope returned and the total background sky counts started to return to the initial trend as can be seen in the last five data points.

Table 4.18 lists the values obtained from the model. The radius of the exoplanet and the inclination angle obtained from the model is consistent with the values reported by Triaud et al. (2015).The radius was determined as $R_p = 0.996^{+0.0278}_{-0.0294}\ R_{\rm Jup}$ and the reported value is $R_p = 0.9990^{+0.0300}_{-0.0310}\ R_{\rm Jup}$. The value obtained for the inclination angle is 89.02 degrees and is also consistent with the reported value: $89.02^{+0.11}_{-0.10}$ degrees. Whilst the calculated stellar density, 3.9702 g/cm^3, is not the exact value reported, it is still consistent with the

reported value, $4.050^{+0.077}_{-0.121}$ g/cm^3.

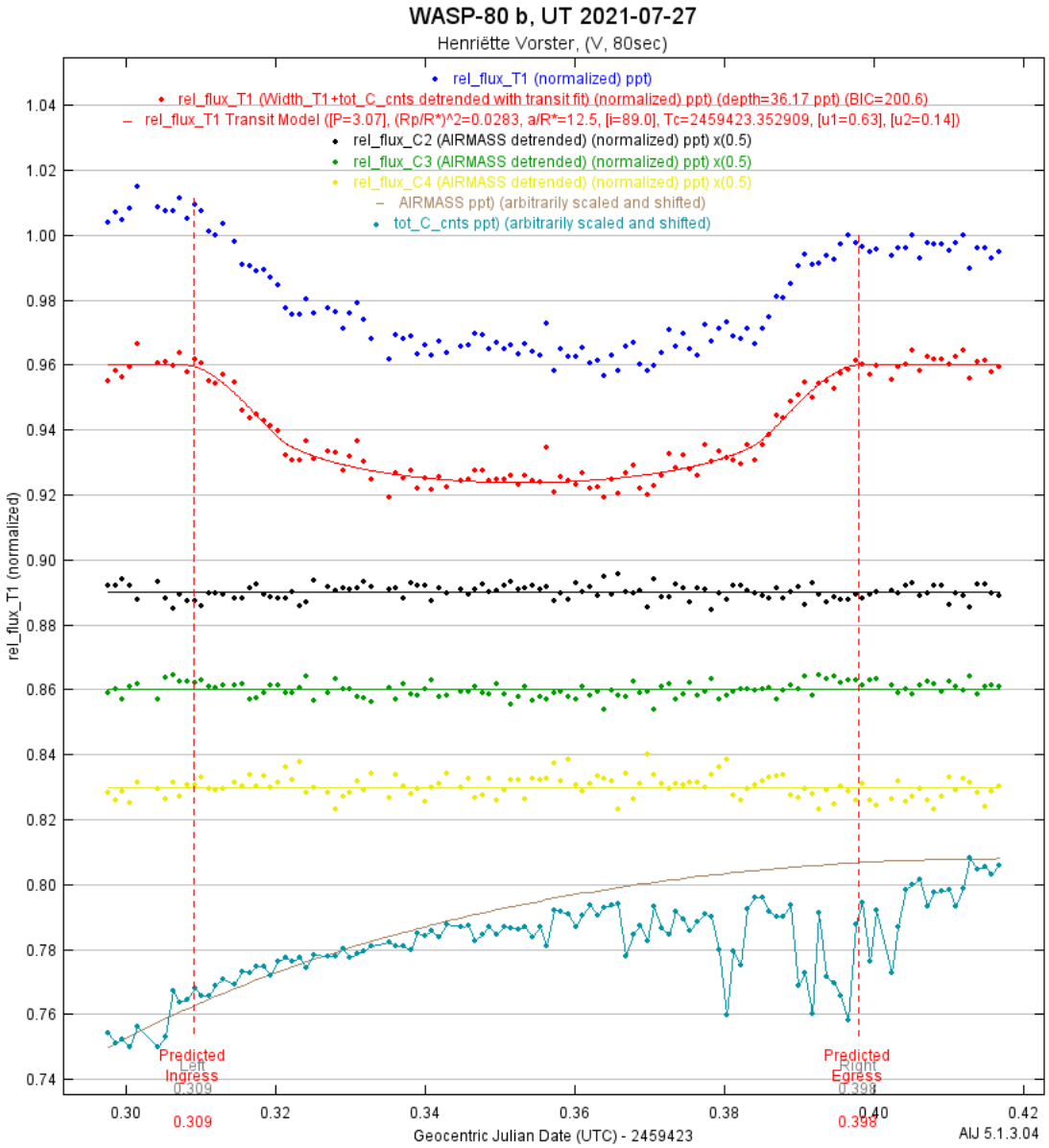

Figure 4.16: WASP-80 b light curve.

The results corresponded very well with the reported values; this was due to various reasons. Firstly since this target had the largest transit depth of all the targets observed and the fact that the target has one of the largest depths ever recorded, it is easier to see the transit event on a light curve, even before a model fit is applied. Secondly, no major problems were encountered with the observation that could have impacted the data negatively and lastly the seeing conditions on the day of the observation were very good, there was little interference from the moon and barely any humidity.

Properties	Units	Calculated Value	Literature Value
R_p	Radius (R_{Jup})	$0.9586^{+0.0278}_{-0.0294}$	$0.9990^{+0.0300}_{-0.0310}$
i	Inclination (deg)	89.02	$89.02^{+0.11}_{-0.10}$
ρ_*	Density (cgs)	3.9702	$4.050^{+0.077}_{-0.121}$
a/R_*		12.5508	$12.63^{+0.08}_{-0.13}$

Table 4.18: Fit results for WASP-80.

4.6 TOI 392.01 b

Since this target is still a candidate exoplanet that has not been confirmed or rejected, not all system properties have been determined. The properties listed in table 4.19 were obtained from the Exoplanet Follow-up Observing Program (ExoFOP) website (`https://exofop.ipac.caltech.edu`). The planet candidates that were identified by the Transiting Exoplanet Survey Satellite (TESS) are presented in the website where the general community can upload their observational data, calculated parameters and notes about candidate planets.

Parameter	Units	Value
P	Period (days)	0.8490649 ± 0.0000002
R_*	Radius ($R_\odot$)	$1.4402900^{+0.0917080}_{-0.0586085}$
System properties		
R_p	Radius (R_{Jup})	1.44 ± 0.08
ρ_*	Density (cgs)	$0.4671417^{+0.1011478}_{-0.1088156}$

Table 4.19: Values for TOI 392.01 parameter and system properties

Unfortunately, during the observation of TOI 392 the drift that was experienced lead to only one comparison star being present in all the images. The light curve obtained from this data is given in figure 4.17. The data was binned with a factor of three since this target had a very low predicted transit depth. The binned data can be seen from the larger red dots in the figure whilst the grey dots represent the data with no binning factor. The resulting model is the same whether the data was binned or not, but since the photometry could not be executed to satisfaction, the resulting model is not a good representation of the transit event. To effectively bin the data together the images have to be combined before aperture photometry is executed; unfortunately this could not be done because the images would not align properly due to the drifting that occurs at the Nooitgedacht telescope.

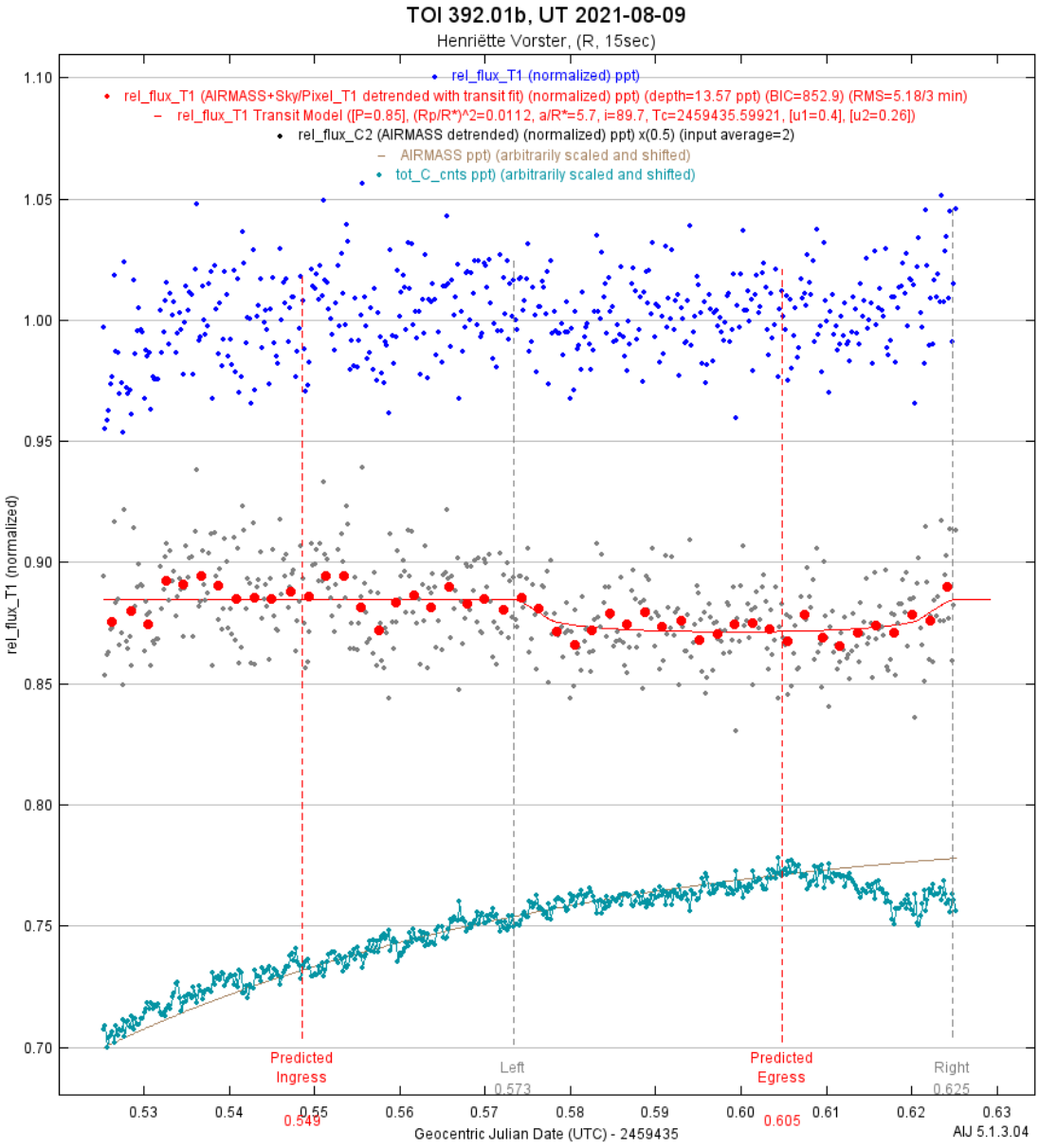

Figure 4.17: TOI 392.01 b light curve.

The data for this target was detrended with the airmass and the background sky counts for the target, which yielded to the lowest BIC-value. As seen in figure 4.17 the predicted ingress- and egress-points are not close to that of the model, and according to the model the duration of the transit is shorter. The properties of the system calculated from the model are listed in table 4.20. Since the photometry could not be completed to satisfaction, the results cannot be trusted.

Properties	Units	Calculated Value	Literature Value
R_p	Radius (R_{Jup})	$1.4821^{+0.0944}_{-0.0603}$	1.44 ± 0.08
i	Inclination (deg)	89.69	
ρ_*	Density (cgs)	4.9366	$0.4671417^{+0.1011478}_{-0.1088156}$
a/R_*		5.7316	

Table 4.20: Fit results for TOI 392.01 b.

4.7 KELT-10 b

The parameters used in the creation of the model are listed in table 4.21. The light curve with the model for this target is shown in figure 4.18. Four comparison stars were used during photometry and their light curves are plotted with a binning factor of two. Since the observation of this target started late, only a few minutes of data was captured before the predicted ingress time. The observation was also concluded too early; this meant that there was not a large quantity of data to create the baseline flux for the target.

Parameter	Units	Value	Reference
P	Period (days)	4.1662739 ± 0.0000063	Kuhn et al. (2016)
R_*	Radius ($R_\odot$)	$1.209^{+0.047}_{-0.035}$	Kuhn et al. (2016)
b		$0.230^{+0.11}_{-0.14}$	Kuhn et al. (2016)
System properties			
R_p	Radius (R_{Jup})	$1.399^{+0.069}_{+0.049}$	Kuhn et al. (2016)
i	Inclination (deg)	$88.61^{+0.86}_{-0.74}$	Kuhn et al. (2016)
ρ_*	Density (cgs)	$0.889^{+0.062}_{-0.088}$	Kuhn et al. (2016)
a/R_*		$9.34^{+0.21}_{-0.32}$	Kuhn et al. (2016)

Table 4.21: Values for KELT-10 parameter and system properties

During the processing of the data it was noticed that the stars in the images trailed a bit due to the auto-guiding making corrections in the position of the telescope mid-exposure; this is the reason why the data for the total background sky counts are so irregular. The aforementioned is also the reason why the total background sky counts were used as a detrend parameter. The other detrend parameters that were used are: the airmass, the shift of the star on both axes, the background sky count for the target star and the meridian flip. The ingress time as per the model is the same as the predicted time, whilst the egress time has shifted to a much earlier time. It is presumed that this error stems from the creation of the baseline flux and the irregular trend in the total background sky counts.

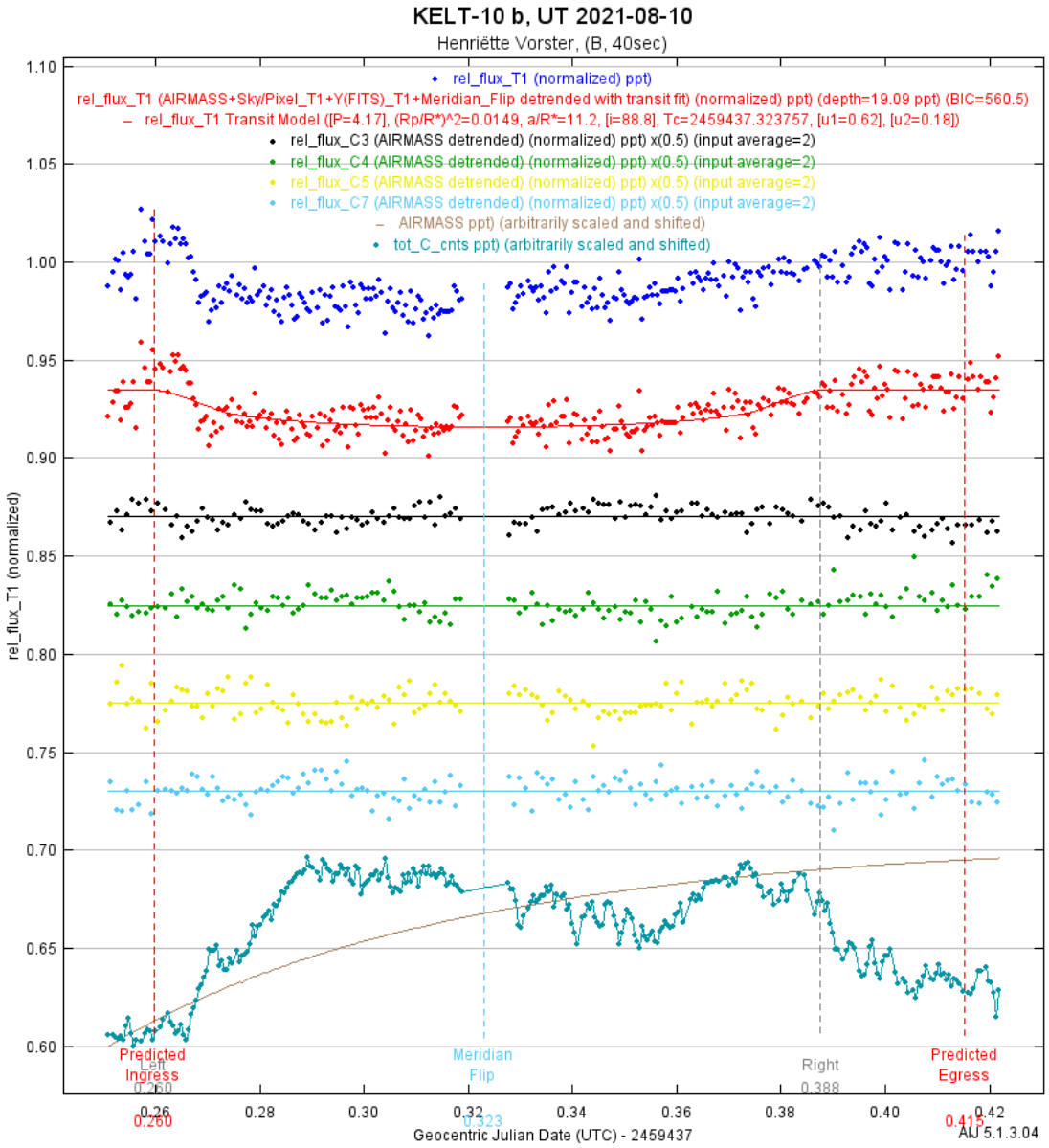

Figure 4.18: KELT-10 b light curve

Properties	Units	Calculated Value	Literature Value
R_p	Radius (R_{Jup})	$1.4342^{+0.0558}_{-0.0415}$	$1.399^{+0.069}_{+0.049}$
i	Inclination (deg)	88.82	$88.61^{+0.86}_{-0.74}$
ρ_*	Density (cgs)	1.5318	$0.889^{+0.062}_{-0.088}$
a/R_*		11.2050	$9.34^{+0.21}_{-0.32}$

Table 4.22: Fit results for KELT-10 b.

The value for the radius of the exoplanet, retrieved from the model, is $R_p = 11.4342^{+0.0558}_{-0.0415}$ R_{Jup} while the reported value is $R_p = 1.399^{+0.069}_{-0.049}$ R_{Jup}. The value from the model is consistent with the reported value. Since the duration of the model does not coincide with the predicted duration, $a/R_* = 11.2050$ was extracted from the model, whilst the reported

value is $a/R_* = 9.34^{+0.21}_{-0.32}$ (Kuhn et al., 2016). From equation 2.4 it is known that a/R_* is dependent on the duration of the transit. Since the inclination angle and stellar density is dependent on the scale of the system, the values for these variables will be inconsistent with the values reported by Kuhn et al. (2016).

Chapter 5

Conclusions

The main motivation for this research study was to discover a minimum threshold for the transit depth that an exoplanet transit event can have, and still be observable from the Nooitgedacht Observatory. During the course of this project many issues came to light, which hindered the process of obtaining data. The benefit to the struggles that were experienced led to a good learning curve on how to handle and overcome the obstacles that came to light. Of the nine observations that were made, only five were deemed successful whilst the other four observations were impeded by either observer or instrumental errors.

This chapter will give a summary of the results that were obtained; possible improvements that could be made at the Nooitgedacht Observatory and final conclusions.

5.1 Data collection

Overall, the data collection for this project went well. The team learnt how to avoid some of the issues that were encountered, such as programming the software to capture a smaller amount of images and adjusting the focus slightly over a period of time, instead of completely refocusing the telescope in order to keep the data viable

For future exoplanet observation, it would be recommended that only one filter be used on faint targets that require longer exposure times, as done for WASP-80 in section 4.5. The aforementioned would increase the amount of data points and led to a better model fit. The opposite of this can be seen in section 4.3, where it was decided to capture the target in all four filters for the sake of wanting to try everything, and ultimately being left with insufficient data. In the event that the observer wanted to capture a faint target in more than one filter, it is suggested that the target be observed on multiple nights if possible, to ensure that sufficient data is collected to obtain the best model fit.

For brighter stars, the maximum amount of filters used should be two. As seen in section 4.1, for the observation made in 2020, two filters were used, which led to a sufficient

amount of data being collected. HAP-P-57, on the other hand, is a fainter star, and was captured in two filters, section 4.4; even though the observation began too late, a better model would have been obtained if the target had been captured using only one filter.

Observations should start an hour prior to the predicted ingress-point as unforeseen circumstances could delay the start of the observation, such as what happened during the observation of HAT-P-57 b, when it was difficult to find the target in a busy field. The observation should also end an hour after the predicted egress-point. This would ensure that the beginning and end of the transit is captured, even if the predicted times were incorrect. Apart from the aforementioned, it is always advantageous to have more data.

More research should be done on a target before an observation is made; as seen in section 4.2 there can be a large deviation between models for different filters. If the classification of the host star is known, an informed decision can be made as to what filter would be most suited for the observation of a specific star.

5.2 Data Reduction and Results

The factors that had the most negative influence on the results were the issues encountered during observations, which led to errors in the data. This included the focus of the telescope, which did not remain constant throughout observations; as well as the drift that occurred, which resulted in only one comparison star being available.

There are other modelling software and programming codes available, which might have more constrictions on the creation of a transit model, and could also probably, yield better results than the AstroImageJ software used during the course of this project. An example of such would be the EXOFASTv2 software which uses "...differential evolution Markov Chain Monte Carlo code" (Eastman et al., 2013), which can fit transits with error scaling, normalisation and fit detrend parameters to the model.

WASP-80 b was the most successful model obtained for this project, it was the target with the largest transit depth, 29.4ppt, and no large issues occurred during the observation. The model used for this project (study) had the same ingress- and egress-points as what was predicted, figure 4.16, the only concern was the total background counts that did not track the trend of the airmass curve towards the end.

The target with the smallest transit depth was TOI 392.01, this target has not yet been confirmed or rejected as an exoplanet and not many properties of this target are known. Since there was only one comparison star present in the images due to the drift that was experienced, the photometry could not be completed to satisfaction and this resulted in an unreliable model.

The target with the next lowest transit depth was WASP-7 b, with a transit depth of 6.7ppt. This data unfortunately also had only one comparison star, but a transit event

can still be seen in the resulting light curve for the B-band (figure 4.5a). Thus it appears that, if the photometry could have been executed with more comparison stars the results would have coincided with the values found in literature.

The results obtained for WASP-74 b were tainted when the telescope was refocused. The results for the I-band data were very promising (figure 4.12); the values obtained from the model (table 4.13) were within the values obtained from Hellier et al. (2015). It is concluded, with cautious optimism, that a 9.8ppt transit depth is a soft limit for the minimum transit depth a transit event can have, and still be observable from Nooitgedacht.

HD 189733 b was observed on three separate occasions, the observation made in 2020 was successful and the model for the B-band curve found an exoplanet radius that was very close to what was reported in literature. The V-band curve did not fare so well since there was a discrepancy between the values for the radius calculated from the model and the value that was reported. The observation in 2021 commenced too late and the ingress of the transit event was not captured, this contributed to the fact that the model's radius did not coincide with the reported value. The data obtained in 2022 for this target yielded the best radius; closest to the reported value. It is interesting to note that the two best models obtained for the target were from data captured with the B-band filter.

HAT-P-57 b was observed in the B- and V-band. Even though an insufficient amount of data was captured before the ingress-point, and the seeing conditions of the night of the observation were not ideal, a model could still be applied to the data and the transit event could be seen in figures 4.14 and 4.15. The results however, did not coincide with the reported literature values, but this was due to the factors mention above as well as the fact that AIJ was not well-suited to model half-transits.

The model did not correspond to the predicted duration of the transit event because the stars trailed in the images captured during the observation of KELT-10 b, and only a few minutes of data was captured before the predicted ingress-point of the transit event. Despite this, the depth of the transit as per the model did yield a similar radius to the reported value.

5.3 Telescope and instrumentation

The data collected at the Nooitgedacht Observatory was severely influenced by several complications encountered during the observations.

Firstly, the pointing and tracking problem, which, collectively, led to two data sets where only one comparison star was present to use during the photometry phase. The aforementioned caused the light curves to be unusable, which meant that no concise conclusions could be drawn.

Multiple unsuccessful pointing solutions were attempted to improve the pointing of the

telescope. It would be advisable to determine whether there are other more suitable software packages that might be better suited to the equipment at Nooitgedacht.

There are plans to establish an internet connection at Nooitgedacht, which will greatly improve the process of diagnosing problems on site. Since the issue with the tracking of the telescope might stem from the issue with the pointing, solving the one problem might very well solve the other. If an internet connection is established, the problem with the computer's system time will also likely not occur again.

The mirror of the telescope that shifts during an observation also caused inaccuracy in the data. Ideally the radial profile of a non-variable star should be consistent in all the images captured during an observation. But due to the focus of the telescope changing, there can be a large change in the radial profile of the target stars in some data sets; this is evident in the images for WASP-74 b (see appendix A). Since the root of the problem might be because the telescope is unbalanced, it would be advisable for an instrument technician to inspect the equipment. This could also unearth problems that might not have been known beforehand.

If the problem stems from the temperature change, which may be shrinking the metallic parts that control the movement of the mirror, the focus would have to be adjusted continuously throughout an observation. TheSkyX software is capable of handling the focusing of the telescope. If the electronic focuser were connected to the computer system, the software could control the focus of the telescope. This would be advantageous for extended observations if the software were set to refocus the telescope every 30 minutes and also after a meridian flip has occurred.

5.4 Final conclusions

The telescope and equipment at the Nooitgedacht Observatory has been proven to be capable of observing exoplanet transits and to obtain good data for exoplanet follow-up observations. There are a few issues that occur when lengthy observations are made, but all of these issues can be amended.

From the results of this project we determined the soft limit for the minimum transit depth to be at approximately 10ppt. This value may even be lowered, the results for WASP-7b had an acceptable transit depth of 6.7ppt, but a more conclusive observation of this or a similar target must first be executed.

When the pointing and tracking of the telescope is in proper working order, the combination of images for transits with a very small depths, to extract better data, can be investigated. This could be done for targets like TOI 392.01 which has a depth of 2.85ppt.

In closing, when the telescope's pointing and tracking issues have been solved, and the telescope is in proper working order, the combination of images for transits with very

small depths, and this includes the ability to extract better data, can be investigated. If successful, it could very well be possible to extract superior data for targets with transit depths lower that 10ppt.

Appendix A

Radial Profiles

The figures below give the graphs of the radial profiles for all the data sets in this project. The aperture and annulus radii that were used during the aperture photometry phase was obtained from these radial profiles. By reason of the gradual shift in focus during an observation, the radial profiles below was obtained from the images in the series where the star seemed most out of focus. This was achieved by scrolling through the images and making a decision on which image the stars seemed the largest compared to all other images. the selected image were used to obtain the radial profile of the target.

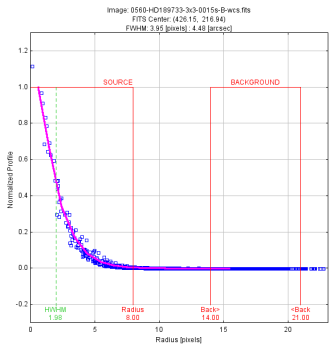

(a) HD 189733 B-band

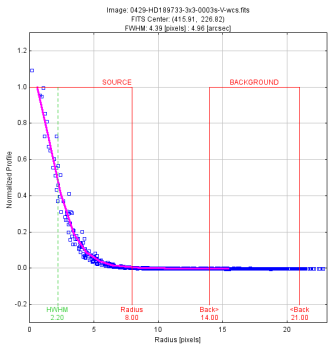

(b) HD 189733 V-band

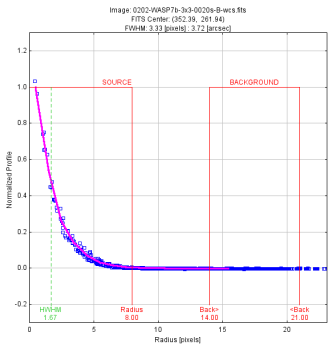

(c) WASP-7 B-band

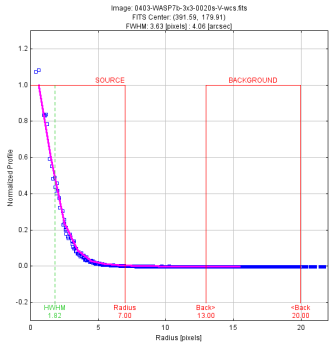

(d) WASP-7 V-band

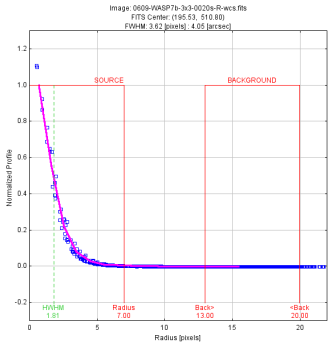

(e) WASP-7 R-band

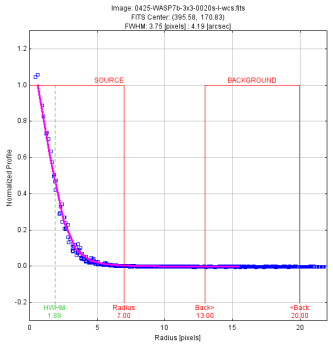

(f) WASP-7 I-band

Figure A.1: Radial profiles

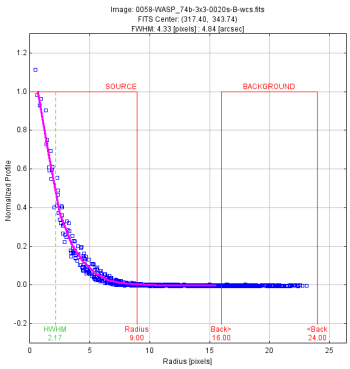

(g) WASP-74 B-band

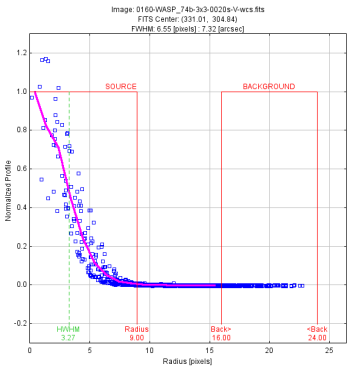

(h) WASP-74 V-band

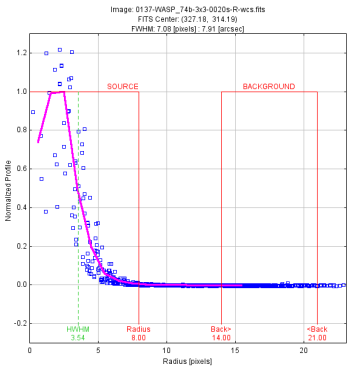

(i) WASP-74 R-band

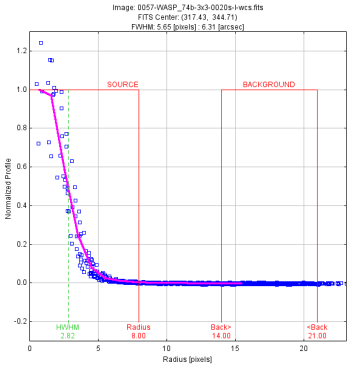

(j) WASP-74 I-band

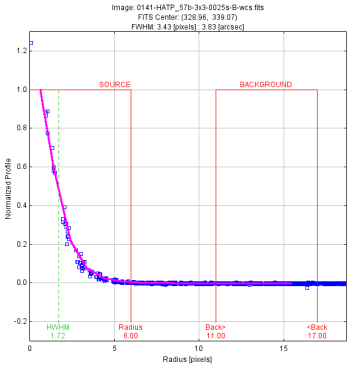

(k) HAT-P-57 B-band

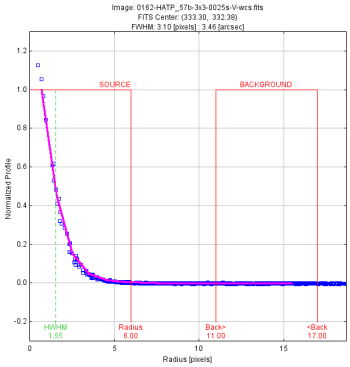

(l) HAT-P-57 V-band

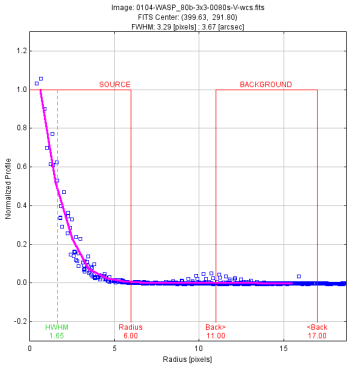

(m) WASP-80 B-band

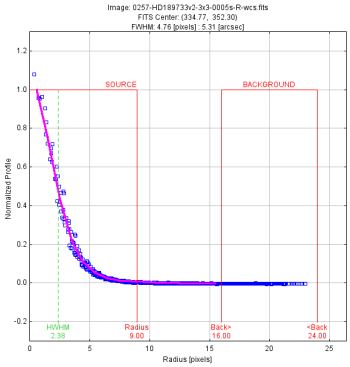

(n) HD 189733 b R-band

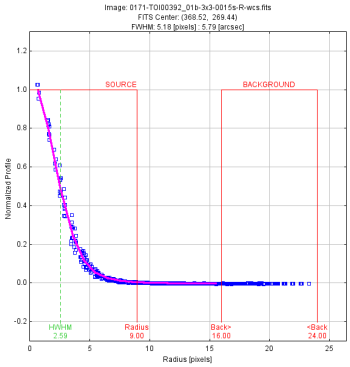

(o) TOI 392.01 R-band

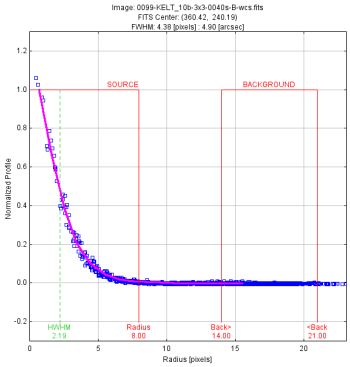

(p) KELT-10 b B-band

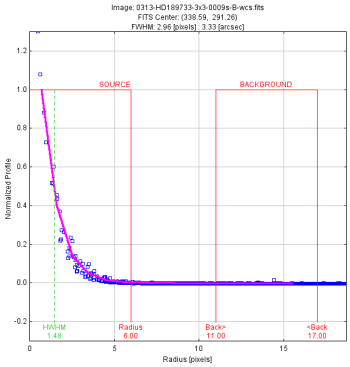

(q) HD 189733 B-band

Figure A.1: Radial profiles (cont.)

The figures below show the difference between the radial profiles for WASP-74 when the images were out of focus (left) and when the focus was restored (right). In the profile for the unfocussed star, a small drop-off at the peak of profile is seen, this was due to the stars appearing as doughnuts when the image ws not focused. When the suggested radii of the focused and unfocused are compared, the differences between them are evident. This is why there are outliers present in the data in figure 4.7, more of the background sky counts are included when the larger aperture size is used on the smaller stars in the focused images.

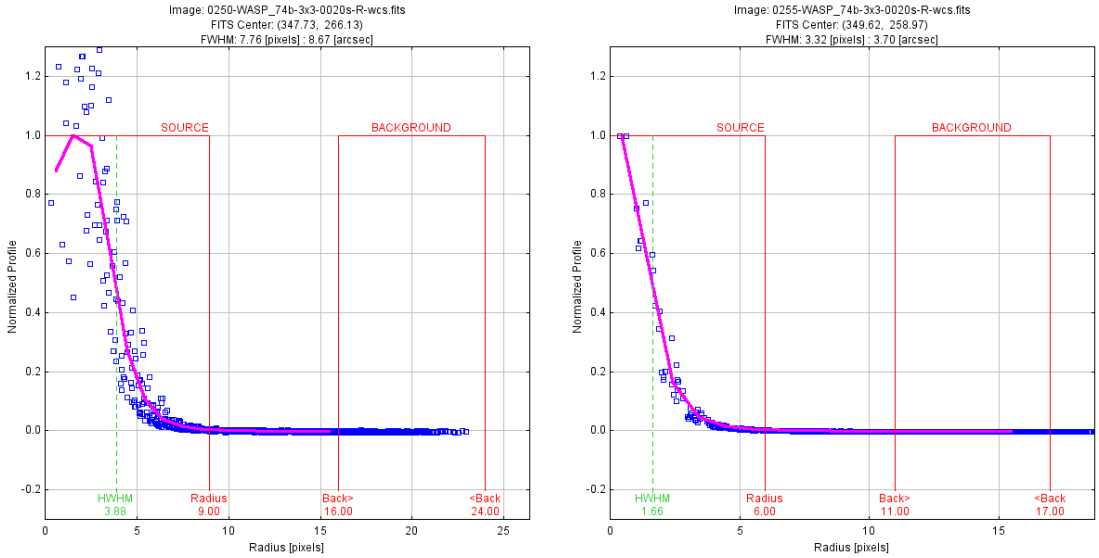

(a) (b)

Figure A.2: WASP-74 R-band

Bibliography

Addison, B., Wright, D. J., Wittenmyer, R. A., Horner, J., Mengel, M. W., Johns, D., Marti, C., Nicholson, B., Soutter, J., Bowler, B., et al. (2019). Minerva-australis. i. design, commissioning, and first photometric results. *Publications of the Astronomical Society of the Pacific*, 131(1005):115003.

Akeson, R., Chen, X., Ciardi, D., Crane, M., Good, J., Harbut, M., Jackson, E., Kane, S., Laity, A., Leifer, S., et al. (2013). The nasa exoplanet archive: data and tools for exoplanet research. *Publications of the Astronomical Society of the Pacific*, 125(930):989.

Bakos, G., Noyes, R., Kovács, G., Stanek, K., Sasselov, D., and Domsa, I. (2004). Wide-field millimagnitude photometry with the hat: A tool for extrasolar planet detection. *Publications of the Astronomical Society of the Pacific*, 116(817):266.

Charbonneau, D., Brown, T. M., Burrows, A., and Laughlin, G. (2006). When extrasolar planets transit their parent stars. *arXiv preprint astro-ph/0603376*.

Charbonneau, D., Brown, T. M., Latham, D. W., and Mayor, M. (1999). Detection of planetary transits across a sun-like star. *The Astrophysical Journal*, 529(1):L45.

Collins, K. A., Kielkopf, J. F., Stassun, K. G., and Hessman, F. V. (2017). Astroimagej: image processing and photometric extraction for ultra-precise astronomical light curves. *The Astronomical Journal*, 153(2):77.

Deeg, H. J. and Alonso, R. (2018). Transit photometry as an exoplanet discovery method. *arXiv preprint arXiv:1803.07867*.

Eastman, J., Gaudi, B. S., and Agol, E. (2013). Exofast: A fast exoplanetary fitting suite in idl. *Publications of the Astronomical Society of the Pacific*, 125(923):83.

Fischer, D. A., Howard, A. W., Laughlin, G. P., Macintosh, B., Mahadevan, S., Sahlmann, J., and Yee, J. C. (2015). Exoplanet detection techniques. *arXiv preprint arXiv:1505.06869*.

Hartman, J. D., Bakos, G., Buchhave, L. A., Torres, G., Latham, D. W., Kovács, G., Bhatti, W., Csubry, Z., de Val-Borro, M., Penev, K., et al. (2015). Hat-p-57b: a short-period giant planet transiting a bright rapidly rotating a8v star confirmed via doppler tomography. *The Astronomical Journal*, 150(6):197.

Haswell, C. A. (2010). *Transiting exoplanets*. Cambridge University Press.

Hellier, C., Anderson, D., Cameron, A. C., Delrez, L., Gillon, M., Jehin, E., Lendl, M., Maxted, P., Pepe, F., Pollacco, D., et al. (2015). Three wasp-south transiting exoplanets: Wasp-74b, wasp-83b, and wasp-89b. *The Astronomical Journal*, 150(1):18.

Henry, G. W., Marcy, G. W., Butler, R. P., and Vogt, S. S. (1999). A transiting "51 peg-like" planet. *The Astrophysical Journal*, 529(1):L41.

Jensen, E. (2013). Tapir: A web interface for transit/eclipse observability. *Astrophysics Source Code Library*, pages ascl–1306.

Kuhn, R. B., Rodriguez, J. E., Collins, K. A., Lund, M. B., Siverd, R. J., Colón, K. D., Pepper, J., Stassun, K. G., Cargile, P. A., James, D. J., et al. (2016). Kelt-10b: the first transiting exoplanet from the kelt-south survey–a hot sub-jupiter transiting a v= 10.7 early g-star. *Monthly Notices of the Royal Astronomical Society*, 459(4):4281–4298.

Lang, D., Hogg, D. W., Mierle, K., Blanton, M., and Roweis, S. (2010). Astrometry. net: Blind astrometric calibration of arbitrary astronomical images. *The astronomical journal*, 139(5):1782.

Marshall, J. and DePoy, D. (2013). Flattening scientific ccd imaging data with a dome flat-field system. *Publications of the Astronomical Society of the Pacific*, 125(932):1277.

Mayor, M. and Queloz, D. (1995). A jupiter-mass companion to a solar-type star. *Nature*, 378(6555):355–359.

Patel, J. A. and Espinoza, N. (2022). Empirical limb-darkening coefficients and transit parameters of known exoplanets from tess. *The Astronomical Journal*, 163(5):228.

Pepper, J., Pogge, R. W., DePoy, D., Marshall, J., Stanek, K., Stutz, A. M., Poindexter, S., Siverd, R., O'Brien, T. P., Trueblood, M., et al. (2007). The kilodegree extremely little telescope (kelt): A small robotic telescope for large-area synoptic surveys. *Publications of the Astronomical Society of the Pacific*, 119(858):923.

Poddanỳ, S., Brát, L., and Pejcha, O. (2010). Exoplanet transit database. reduction and processing of the photometric data of exoplanet transits. *New Astronomy*, 15(3):297–301.

Pollacco, D. L., Skillen, I., Cameron, A. C., Christian, D., Hellier, C., Irwin, J., Lister, T., Street, R., West, R. G., Anderson, D., et al. (2006). The wasp project and the superwasp cameras. *Publications of the Astronomical Society of the Pacific*, 118(848):1407.

Ricker, G. R., Winn, J. N., Vanderspek, R., Latham, D. W., Bakos, G. Á., Bean, J. L., Berta-Thompson, Z. K., Brown, T. M., Buchhave, L., Butler, N. R., et al. (2014). Transiting exoplanet survey satellite. *Journal of Astronomical Telescopes, Instruments, and Systems*, 1(1):014003.

Schneider, J. (2007). The extrasolar planets encyclopaedia. *http://exoplanet. eu*.

Seager, S. and Mallen-Ornelas, G. (2003). A unique solution of planet and star parameters from an extrasolar planet transit light curve. *The Astrophysical Journal*, 585(2):1038.

Sing, D. K. (2018). Observational techniques with transiting exoplanetary atmospheres. In *Astrophysics of Exoplanetary Atmospheres*, pages 3–48. Springer.

Southworth, J., Dominik, M., Jørgensen, U., Rahvar, S., Snodgrass, C., Alsubai, K., Bozza, V., Browne, P., Burgdorf, M., Novati, S. C., et al. (2011). A much lower density for the transiting extrasolar planet wasp-7. *Astronomy & Astrophysics*, 527:A8.

Triaud, A. H., Anderson, D., Cameron, A. C., Doyle, A., Fumel, A., Gillon, M., Hellier, C., Jehin, E., Lendl, M., Lovis, C., et al. (2013). Wasp-80b: a gas giant transiting a cool dwarf. *Astronomy & Astrophysics*, 551:A80.

Triaud, A. H., Gillon, M., Ehrenreich, D., Herrero, E., Lendl, M., Anderson, D. R., Collier Cameron, A., Delrez, L., Demory, B.-O., Hellier, C., et al. (2015). Wasp-80b has a dayside within the t-dwarf range. *Monthly Notices of the Royal Astronomical Society*, 450(3):2279–2290.